Available online at www.sciencedirect.com
SCIENCE DIRECT®
International Journal of Plasticity 21 (2005) 1061–1096
INTERNATIONAL JOURNAL OF Plasticity
www.elsevier.com/locate/ijplas

Analysis of the spallation mechanism suppression in plasma-sprayed TBCs through the use of heterogeneous bond coat architectures

Marek-Jerzy Pindera [a,*], Jacob Aboudi [b], Steven M. Arnold [c]

[a] *Department of Civil Engineering and Applied Mechanics Group, University of Virginia, Thornton Hall, P.O. Box 400742, Charlottesville, VA 22904, USA*
[b] *Tel-Aviv University, Ramat-Aviv 69978, Israel*
[c] *NASA Glenn Research Center, Cleveland, OH 44135, USA*

Received 30 October 2003; in final revised form 14 February 2004
Available online 26 November 2004

Abstract

This paper critically examines the use of heterogeneous bond coats to increase the durability of plasma-sprayed thermal barrier coatings under spatially-uniform cyclic thermal loading. A major failure mechanism in these types of coatings involves spallation of the top coat caused by the top/bond coat thermal expansion mismatch concomitant with deposition-induced top/bond coat interfacial roughness, oxide film growth and creep-induced normal stress reversal at the rough interface's peaks. The reduction of the top/bond coat thermal expansion mismatch aimed at increasing coating durability can be achieved by embedding alumina particles in the bond coat. Herein, we analyze the evolution of local stress and inelastic strain fields in the vicinity of the rough top/bond coat interface during thermal cycling, and how these fields are influenced by the presence of spatially uniform and non-uniform (graded) distributions of alumina particles in the metallic bond coat. The analysis is conducted using the *higher-order theory for functionally graded materials* which accounts for the high-temperature creep/relaxation effects within the individual TBC constituents. In the presence of two-phase bond coat microstructures, both the actual and homogenized bond coat properties are employed in the

* Corresponding author. Tel.: +1 804 924 1040; fax: +1 804 982 2951.
E-mail address: mp3g@virginia.edu (M.-J. Pindera).

0749-6419/$ - see front matter
doi:10.1016/j.ijplas.2004.02.004

analysis in order to highlight the limitations of the prevalent homogenization-based approach applied to graded materials. The results reveal that the use of heterogeneous, two-phase bond coats, with spatially uniform or graded microstructures, while slightly suppressing the normal stress component evolution in the interfacial peak region, increases the magnitude of the shear stress component as well as the inelastic strain evolution in this region, thereby potentially promoting delamination initiation. The analysis based on homogenized bond coat microstructure produces misleading results relative to how the bond coat heterogeneity affects the magnitude of the normal and shear stress, and inelastic strain, components.

1. Introduction

Thermal barrier coatings (TBCs) are employed on structural components exposed to large thermal gradients in order to enable them to operate at higher temperatures or to operate longer at a given service temperature. In the case of nickel-based structural components employed in the hot section of aircraft gas turbine engines, zirconia-based coatings are typically used due to the low thermal conductivity of zirconia and its chemical stability at elevated temperatures. These coatings consist of a zirconia top coat and a nickel-based bond coat. The bond coat improves the thermomechanical compatibility between the top coat and the substrate, and is first deposited onto the substrate material, followed by the top coat itself. In oxidizing environments at elevated temperatures, the bond coat alloy composition produces a thin oxide film (called thermally-grown oxide or TGO) at the top coat/bond coat interface which acts as a protective oxidation barrier.

There are two ways of depositing the bond and top coats onto the substrate, using either plasma-spray or electron-beam physical vapor-deposition process, as discussed by Strangman (1985) and Sheffler and Gupta (1988). In this investigation, we model plasma-sprayed TBCs. The plasma-spray deposition process produces a coating with microstructure characterized by porosities and microcracks, and a rough top/bond coat interface whose strength is relatively low due to primarily mechanical interlocking mechanism. The porous microstructure results in low thermal conductivity, inelastic creep-like behavior suggested to be due to sliding of the rough microcrack interfaces, DiMassi-Marcin et al. (1990), and low out-of-plane mechanical moduli and strength. A major failure mechanism for plasma-sprayed coatings is the spallation of the top coat from the bond coat which generally initiates at or just above the top coat/TGO interface, as demonstrated experimentally by Miller and Lowell (1982). The failure mechanism was hypothesized to involve peel stress normal to the top/bond coat interface induced into the coating during the cooldown stage of a thermal cycle due to the thermal expansion mismatch between the top coat and the bond coat, and was shown to be influenced by interfacial oxide film formation during exposure to elevated temperatures. Based on the observed location of delamination, the interface's irregularity was hypothesized to play a role.

The influence of rough interface, oxide film, and thermomechanical property mismatch on the spallation mechanism has been subsequently studied by a number of

investigators (cf. Evans et al., 1983; Chang et al., 1987; Petrus and Ferguson, 1997; Freborg et al., 1998; Pindera et al., 2000; Ali et al., 2001). These studies demonstrated the evolution of a non-zero stress component normal to the interface during cyclic thermal loading. Due to stress relaxation during the hold period of a heatup–hold–cooldown thermal cycle, this stress component becomes tensile at the interface's crest upon cooldown, setting up a delamination initiation site at this location. In the trough region, the normal stress becomes compressive, due also to stress relaxation. The growth of the oxide film at the top coat/bond coat interface subsequently changes the normal stress sign in the trough region, facilitating horizontal delamination growth. This model has been proposed by a number of investigators to explain the initiation and growth of delamination at or just above the top coat/oxide film interface, ultimately leading to spallation.

The above investigations also demonstrated that the top/bond coat thermal expansion mismatch has the greatest effect on the evolution of the normal stress at the rough top/bond coat interface. In order to reduce this mismatch, and thus increase coating durability, Brindley et al. (1998) fabricated TBCs with heterogeneous bond coats consisting of a uniform dispersion of submicron alumina particles in the nickel-based alloy bond coats. Durability experiments subsequently demonstrated consistent doubling of TBC life with just a 5% alumina content. Bond coats with up to 20% alumina content were also fabricated and tested, but showed substantial variability in durability due to oxidation problems currently being addressed through improved deposition techniques.

Motivated by the results of Brindley et al. (1998), we critically examine the potential suppression of spallation mechanism through the use of heterogeneous bond coat microstructures. The objective is to better understand, in mechanics terms, the evolution of stress and inelastic strain fields in plasma-sprayed TBCs with rough interfaces and heterogeneous bond coats subjected to spatially uniform thermal cyclic loading that simulates furnace durability test. The impact of the oxide film evolution is not considered here, but has been reported elsewhere and will be briefly discussed at the appropriate place later. The analysis of thermally-induced stresses in TBCs with heterogeneous bond coats is conducted using the *higher-order theory for functionally graded materials*, summarized in the comprehensive review article by Aboudi et al. (1999). This analysis, which accounts for the important creep/relaxation effects within the individual TBC constituents, is conducted in two distinct ways which reflect the present dichotomy in the modeling of heterogeneous materials. The coupled approach explicitly accounts for the micro-macrostructural interaction arising from the heterogeneous bond coat microstructure and is an intrinsic feature of the higher-order theory. The uncoupled approach, which is the prevailing paradigm in the mechanics/materials communities, replaces the heterogeneous bond coat microstructure by fictitious homogenized properties determined locally using the chosen micromechanics model, Pindera et al. (1995). Comparison of stress and inelastic strain fields generated using both methods allows us to examine the applicability of the homogenization-based approach in analyzing the response of the considered TBCs, and the limitation of the conclusions based on this approach vis-a-vis coating durability enhancement through the use of heterogeneous bond coats.

2. Outline of the higher-order theory for FGMs

The higher-order theory for functionally graded materials is an approximate analytical approach, demonstrated to be sufficiently accurate in comparison with results obtained from more detailed finite-element analyses, for modeling stress and deformation fields in heterogeneous materials with different microstructural details. It circumvents the yet-to-be resolved problem of local homogenization of the material's spatially-variable heterogeneous microstructure, based on the concept of a representative volume element, by explicitly accounting for the microstructural details and local particle–particle interactions in the course of obtaining approximate analytical solutions for the local field quantities. This is accomplished by discretizing the volume occupied by a heterogeneous material into subvolumes in a manner that mimics the material's microstructure. The geometric model of a heterogeneous material that provides the basis for the higher-order theory's construction is shown in Fig. 1. The material may be reinforced by an arbitrary distribution of continuous fibers or finite-length inclusions in the x_2–x_3 plane, continuously or periodically arranged in the direction of the x_1 axis. The heterogeneous microstructure in the x_2–x_3 plane is discretized into N_q and N_r generic cells in the intervals $0 \leqslant x_2 \leqslant H$, $0 \leqslant x_3 \leqslant L$, respectively. The indices q and r, whose ranges are $q = 1, 2, \ldots, N_q$ and $r = 1, 2, \ldots, N_r$, identify the generic cell in the x_2–x_3 plane. The generic cell (q,r) consists of eight subcells designated by the triplet $(\alpha\beta\gamma)$, where each index α, β, γ takes on the values 1 or 2 which indicate the relative position of the given subcell along the x_1, x_2 and x_3 axis,

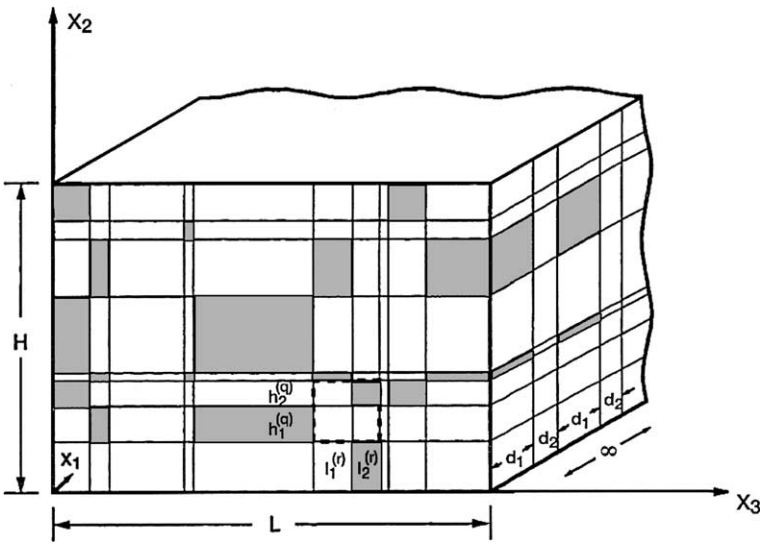

Fig. 1. A geometric model of a material functionally graded material in the x_2–x_3 plane with periodicity in the x_1 direction, illustrating the volume discretization employed in the higher-order theory based on generic cells (highlighted by dashed lines) subdivided into eight subcells.

respectively. The dimensions of the generic cell along the periodic x_1 direction, d_1 and d_2 are fixed, whereas the dimensions along the non-periodic directions x_2 and x_3, $h_1^{(q)}$,$h_2^{(q)}$, and $l_1^{(r)}$,$l_2^{(r)}$, can vary arbitrarily such that

$$H = \sum_{q=1}^{N_q}(h_1^{(q)} + h_2^{(q)}) \qquad L = \sum_{r=1}^{N_r}(l_1^{(r)} + l_2^{(r)}). \tag{1}$$

The applied loading may involve an arbitrary temperature or heat flux distribution and mechanical effects represented by a combination of surface displacements, their normal derivatives, and tractions in the x_2–x_3 plane, and a uniform strain in the x_1 direction. For the prescribed loading, an approximate solution for the temperature and displacement fields within each $(\alpha\beta\gamma)$ subcell, referred to the local coordinate system $\bar{x}_1^{(\alpha)}$–$\bar{x}_2^{(\beta)}$–$\bar{x}_3^{(\gamma)}$ placed at the subcell's centroid, is constructed in two steps using volume and surface averaging procedures described next. The solution methodology outline is sufficiently concise to facilitate interpretation of the presented results, but avoids the lengthy derivations of the governing equations for the local field variables within the subvolumes of the discretized microstructure described in detail elsewhere (cf. Aboudi et al., 1999).

2.1. Thermal analysis

Under steady-state temperature or heat flux distributions applied in the x_2–x_3 plane at the boundaries of the geometric model shown in Fig. 1, the heat flux in each $(\alpha\beta\gamma)$ subcell of every (q,r)th generic cell must satisfy the heat conduction equation,

$$\frac{\partial q_1^{(\alpha\beta\gamma)}}{\partial \bar{x}_1^{(\alpha)}} + \frac{\partial q_2^{(\alpha\beta\gamma)}}{\partial \bar{x}_2^{(\beta)}} + \frac{\partial q_3^{(\alpha\beta\gamma)}}{\partial \bar{x}_3^{(\gamma)}} = 0, \quad (\alpha,\beta,\gamma = 1,2). \tag{2}$$

The subcell heat flux components $q_i^{(\alpha\beta\gamma)}$ are obtained from the temperature field using Fourier's conduction law,

$$q_i^{(\alpha\beta\gamma)} = -k^{(\alpha\beta\gamma)}\frac{\partial T^{(\alpha\beta\gamma)}}{\partial \bar{x}_i^{(\cdot)}}, \tag{3}$$

where $k^{(\alpha\beta\gamma)}$ are the coefficients of heat conductivity of the material in the $(\alpha\beta\gamma)$ subcell, and no summation is implied by repeated Greek letters. The temperature distribution $T^{(\alpha\beta\gamma)}$ in the $(\alpha\beta\gamma)$ subcell of the (q,r)th generic cell is then approximated by a second-order expansion in the local coordinates $\bar{x}_1^{(\alpha)}$, $\bar{x}_2^{(\beta)}$, $\bar{x}_3^{(\gamma)}$ as follows,

$$\begin{aligned} T^{(\alpha\beta\gamma)} = {} & T_{(000)}^{(\alpha\beta\gamma)} + \bar{x}_2^{(\beta)}T_{(010)}^{(\alpha\beta\gamma)} + \bar{x}_3^{(\gamma)}T_{(001)}^{(\alpha\beta\gamma)} + \frac{1}{2}\left(3\bar{x}_1^{(\alpha)2} - \frac{d_\alpha^2}{4}\right)T_{(200)}^{(\alpha\beta\gamma)} \\ & + \frac{1}{2}\left(3\bar{x}_2^{(\beta)2} - \frac{h_\beta^{(q)2}}{4}\right)T_{(020)}^{(\alpha\beta\gamma)} + \frac{1}{2}\left(3\bar{x}_3^{(\gamma)2} - \frac{l_\gamma^{(r)2}}{4}\right)T_{(002)}^{(\alpha\beta\gamma)}, \end{aligned} \tag{4}$$

where the unknown volume-averaged temperature $T_{(000)}^{(\alpha\beta\gamma)}$, and the higher-order coefficients $T_{(lmn)}^{(\alpha\beta\gamma)}$ (l, m, n = 0, 1, or 2 with $l + m + n \leqslant 2$), are determined in the manner described below.

Given the six unknown quantities associated with each subcell (i.e., $T^{(\alpha\beta\gamma)}_{(000)},\ldots,T^{(\alpha\beta\gamma)}_{(002)}$) and eight subcells within each generic cell, $48N_qN_r$ unknown quantities must be determined for a composite with N_q rows and N_r columns of cells containing arbitrarily specified materials. These quantities are determined by first satisfying the local heat conduction equation, Eq. (2), in each subcell in a volumetric sense. To this end, the following volume-averaged fluxes are defined

$$Q^{(\alpha\beta\gamma)}_{i(l,m,n)} = \frac{1}{v^{(q,r)}_{(\alpha\beta\gamma)}} \int_{-d_\alpha/2}^{d_\alpha/2} \int_{-h^{(q)}_\beta/2}^{h^{(q)}_\beta/2} \int_{-l^{(r)}_\gamma/2}^{l^{(r)}_\gamma/2} (\bar{x}^{(\alpha)}_1)^l (\bar{x}^{(\beta)}_2)^m (\bar{x}^{(\gamma)}_3)^n q^{(\alpha\beta\gamma)}_i \, \mathrm{d}\bar{x}^{(\alpha)}_1 \, \mathrm{d}\bar{x}^{(\beta)}_2 \, \mathrm{d}\bar{x}^{(\gamma)}_3, \quad (5)$$

where $v^{(q,r)}_{(\alpha\beta\gamma)} = d_\alpha h^{(q)}_\beta l^{(r)}_\gamma$ is the volume of the $(\alpha\beta\gamma)$ subcell in the (q,r)th generic cell. $Q^{(\beta\gamma)}_{i(0,0,0)}$ is the average value of the heat flux component $q^{(\alpha\beta\gamma)}_i$ in the $(\alpha\beta\gamma)$ subcell, whereas higher-order heat fluxes are obtained for other values of l, m and n. Satisfaction of the heat conduction equation in the volumetric sense results in the following conditions in terms of the volume-averaged flux quantities

$$\left[Q^{(\alpha\beta\gamma)}_{1(1,0,0)}/d^2_\alpha + Q^{(\alpha\beta\gamma)}_{2(0,1,0)}/h^2_\beta + Q^{(\alpha\beta\gamma)}_{3(0,0,1)}/l^2_\gamma\right]^{(q,r)} = 0, \quad (6)$$

which can be expressed in terms of the microvariables $T^{(\alpha\beta\gamma)}_{(lmn)}$ using Eqs. (4) and (5).

Subsequently, continuity of *both* the heat flux and temperature is imposed in a surface-average sense at the interfaces separating adjacent subcells, as well as neighboring cells. For instance, the heat flux continuity at the interfaces separating adjacent subcells within the generic cell (q,r) in the x_2 direction is imposed as follows

$$\frac{1}{l^{(r)}_\gamma} \int_{-l^{(r)}_\gamma/2}^{l^{(r)}_\gamma/2} \left[q^{(\alpha 1\gamma)}_2(h^{(q)}_1/2,\bar{x}^{(\gamma)}_3)\right]^{(q,r)} \mathrm{d}\bar{x}^{(\gamma)}_3 = \frac{1}{l^{(r)}_\gamma} \int_{-l^{(r)}_\gamma/2}^{l^{(r)}_\gamma/2} \left[q^{(\alpha 2\gamma)}_2(-h^{(q)}_2/2,\bar{x}^{(\gamma)}_3)\right]^{(q,r)} \mathrm{d}\bar{x}^{(\gamma)}_3, \quad (7)$$

with similar expressions for the heat flux continuity at the interfaces between adjacent generic cells. Satisfaction of the heat flux continuity in the remaining directions is carried out in the same manner. The resulting conditions are obtained in terms of the volume-averaged heat fluxes of different orders, which are then expressed in terms of the microvariables $T^{(\alpha\beta\gamma)}_{(lmn)}$. For example, the above continuity condition can be shown to reduce to the following expression after some algebraic manipulations,

$$\left[-12Q^{(\alpha 1\gamma)}_{2(0,1,0)}/h_1 + Q^{(\alpha 2\gamma)}_{2(0,0,0)} - 6Q^{(\alpha 2\gamma)}_{2(0,1,0)}/h_2\right]^{(q,r)} - \left[Q^{(\alpha 2\gamma)}_{2(0,0,0)} + 6Q^{(\alpha 2\gamma)}_{2(0,1,0)}/h_2\right]^{(q-1,r)} = 0. \quad (8)$$

Alternatively, the imposition of temperature continuity in the same surface-averaged sense as above between adjacent subcells within each generic cell, as well as between adjacent generic cells, generates a system of equations expressed directly in terms of the microvariables $T^{(\alpha\beta\gamma)}_{(lmn)}$.

Fulfillment of these field equations and continuity conditions in the interior, together with the imposed surface-averaged thermal boundary conditions, provides

the necessary $48N_qN_r$ equations for the $48N_qN_r$ unknown coefficients $T^{(\alpha\beta\gamma)}_{(lmn)}$ in the temperature field expansion in each $(\alpha\beta\gamma)$ subcell. The boundary conditions can be specified in terms of surface-averaged temperatures or heat fluxes on the external surfaces of boundary subcells. For instance, for cells located on the boundaries defined by the indices $q = 1$, N_q, the surface-averaged temperature boundary conditions are

$$\frac{1}{l^{(r)}_\gamma}\int_{-l^{(r)}_\gamma/2}^{l^{(r)}_\gamma/2}\left[T^{(\alpha 1\gamma)}(-h^{(1)}_1/2,\bar{x}^{(\gamma)}_3)\right]^{(1,r)}\mathrm{d}\bar{x}^{(\gamma)}_3 = T^{(r)}_{\mathrm{bottom}}(x_3), \tag{9}$$

$$\frac{1}{l^{(r)}_\gamma}\int_{-l^{(r)}_\gamma/2}^{l^{(r)}_\gamma/2}\left[T^{(\alpha 2\gamma)}(h^{(N_q)}_2,\bar{x}^{(\gamma)}_3)\right]^{(N_q,r)}\mathrm{d}\bar{x}^{(\gamma)}_3 = T^{(r)}_{\mathrm{top}}(x_3), \tag{10}$$

where $T^{(r)}_{\mathrm{bottom}}(x_3)$ and $T^{(r)}_{\mathrm{top}}(x_3)$ are the piece-wise uniform temperatures specified on the horizontal boundaries of the heterogeneous material in the x_2–x_3 plane (see Fig. 1), with similar expressions for the remaining boundaries. The final form of the system of equations assembled using the above equations and conditions can be symbolically written as

$$\boldsymbol{\kappa}\mathbf{T} = \mathbf{t}, \tag{11}$$

where the structural thermal conductivity matrix $\boldsymbol{\kappa}$ contains information on the geometry and thermal conductivities of the individual $(\alpha\beta\gamma)$ subcells in the N_qN_r cells spanning the x_2 and x_3 directions, the thermal coefficient vector $\mathbf{T}$ contains the unknown coefficients that describe the temperature field in each subcell, i.e.,

$$\mathbf{T} = [\mathbf{T}^{(111)}_{11},\ldots,\mathbf{T}^{(222)}_{N_qN_r}],$$

where

$$\mathbf{T}^{(\alpha\beta\gamma)}_{qr} = [T_{(000)},T_{(010)},T_{(001)},T_{(200)},T_{(020)},T_{(002)}]^{(\alpha\beta\gamma)}_{qr}$$

and the thermal force vector $\mathbf{t}$ contains information on the thermal boundary conditions.

2.2. Mechanical analysis

Given the temperature field generated by the applied surface temperatures and/or heat fluxes obtained in the preceding section, the resulting displacement and stress fields are then determined. This is carried out for arbitrary mechanical loading, consistent with global equilibrium requirements, applied to the surfaces of the heterogeneous material.

The stress field in each $(\alpha\beta\gamma)$ subcell of every (q,r)th generic cell produced by the temperature field and specified mechanical loading must satisfy the equilibrium equations

$$\frac{\partial\sigma^{(\alpha\beta\gamma)}_{1j}}{\partial\bar{x}^{(\alpha)}_1}+\frac{\partial\sigma^{(\alpha\beta\gamma)}_{2j}}{\partial\bar{x}^{(\beta)}_2}+\frac{\partial\sigma^{(\alpha\beta\gamma)}_{3j}}{\partial\bar{x}^{(\gamma)}_3}=0,\quad (j=1,2,3). \tag{12}$$

The subcell stress components $\sigma^{(\alpha\beta\gamma)}_{ij}$ are obtained from the inelastic version of Hooke's law (assuming isotropic phases)

$$\sigma_{ij}^{(\alpha\beta\gamma)} = 2\mu^{(\alpha\beta\gamma)}\varepsilon_{ij}^{(\alpha\beta\gamma)} + \lambda^{(\alpha\beta\gamma)}\varepsilon_{kk}^{(\alpha\beta\gamma)}\delta_{ij} - 2\mu^{(\alpha\beta\gamma)}\varepsilon_{ij}^{\mathrm{in}(\alpha\beta\gamma)} - \sigma_{ij}^{\mathrm{T}(\alpha\beta\gamma)}, \tag{13}$$

where $\lambda^{(\alpha\beta\gamma)}$ and $\mu^{(\alpha\beta\gamma)}$ are Lamé's constants of the material filling the given $(\alpha\beta\gamma)$ subcell, $\varepsilon_{ij}^{\mathrm{in}(\alpha\beta\gamma)}$ are inelastic strain components, and $\sigma_{ij}^{\mathrm{T}(\alpha\beta\gamma)}$ are thermal stresses consisting of the products of stiffness tensor components, thermal expansion coefficients and temperature change. The subcell strain components are then obtained from the strain–displacement relations. The inclusion of inelastic effects in the present formulation is sufficiently general to admit either incremental plasticity, power-law creep or unified viscoplasticity constitutive models.

The displacement field in the subcell $(\alpha\beta\gamma)$ of the (q,r)th generic cell is approximated by a second-order expansion in the local coordinates $\bar{x}_1^{(\alpha)}$, $\bar{x}_2^{(\beta)}$, and $\bar{x}_3^{(\gamma)}$ as follows,

$$u_1^{(\alpha\beta\gamma)} = W_{1(000)}^{(\alpha\beta\gamma)} + \bar{x}_1^{(\alpha)} W_{1(100)}^{(\alpha\beta\gamma)}, \tag{14}$$

$$\begin{aligned} u_2^{(\alpha\beta\gamma)} = {} & W_{2(000)}^{(\alpha\beta\gamma)} + \bar{x}_2^{(\beta)} W_{2(010)}^{(\alpha\beta\gamma)} + \bar{x}_3^{(\gamma)} W_{2(001)}^{(\alpha\beta\gamma)} + \frac{1}{2}\left(3\bar{x}_1^{(\alpha)2} - \frac{d_\alpha^2}{4}\right) W_{2(200)}^{(\alpha\beta\gamma)} \\ & + \frac{1}{2}\left(3\bar{x}_2^{(\beta)2} - \frac{h_\beta^{(q)2}}{4}\right) W_{2(020)}^{(\alpha\beta\gamma)} + \frac{1}{2}\left(3\bar{x}_3^{(\gamma)2} - \frac{l_\gamma^{(r)2}}{4}\right) W_{2(002)}^{(\alpha\beta\gamma)}, \end{aligned} \tag{15}$$

$$\begin{aligned} u_3^{(\alpha\beta\gamma)} = {} & W_{3(000)}^{(\alpha\beta\gamma)} + \bar{x}_2^{(\beta)} W_{3(010)}^{(\alpha\beta\gamma)} + \bar{x}_3^{(\gamma)} W_{3(001)}^{(\alpha\beta\gamma)} + \frac{1}{2}\left(3\bar{x}_1^{(\alpha)2} - \frac{d_\alpha^2}{4}\right) W_{3(200)}^{(\alpha\beta\gamma)} \\ & + \frac{1}{2}\left(3\bar{x}_2^{(\beta)2} - \frac{h_\beta^{(q)2}}{4}\right) W_{3(020)}^{(\alpha\beta\gamma)} + \frac{1}{2}\left(3\bar{x}_3^{(\gamma)2} - \frac{l_\gamma^{(r)2}}{4}\right) W_{3(002)}^{(\alpha\beta\gamma)}, \end{aligned} \tag{16}$$

where the microvariables $W_{i(lmn)}^{(\alpha\beta\gamma)}$ have similar interpretation as the corresponding thermal microvariables for different values of l, m and n. In the presence of inelastic effects, the chosen form of the displacement field implies that these microvariables depend implicitly on the inelastic strain distributions. This, in turn, gives rise to a higher-order stress field in contrast to the linear stress field obtained from the corresponding displacement field representation with constant coefficients. This higher-order stress field is represented by a higher-order Legendre polynomial expansion in the local coordinates. Therefore, the strain field generated from the assumed displacement field, and the resulting mechanical and thermal stress fields, are also be expressed in terms of Legendre polynomials:

$$\varepsilon_{ij}^{(\alpha\beta\gamma)} = \sum_{l=0}^{1}\sum_{m=0}^{1}\sum_{n=0}^{1}\sqrt{(1+2l)(1+2m)(1+2n)}\, e_{ij(l,m,n)}^{(\alpha\beta\gamma)} P_l(\zeta_1^{(\alpha)}) P_m(\zeta_2^{(\beta)}) P_n(\zeta_3^{(\gamma)}), \tag{17}$$

$$\sigma_{ij}^{(\alpha\beta\gamma)} = \sum_{l=0}^{\infty}\sum_{m=0}^{\infty}\sum_{n=0}^{\infty}\sqrt{(1+2l)(1+2m)(1+2n)}\, \tau_{ij(l,m,n)}^{(\alpha\beta\gamma)} P_l(\zeta_1^{(\alpha)}) P_m(\zeta_2^{(\beta)}) P_n(\zeta_3^{(\gamma)}), \tag{18}$$

$$\sigma_{ij}^{\mathrm{T}(\alpha\beta\gamma)} = \sum_{l=0}^{2}\sum_{m=0}^{2}\sum_{n=0}^{2}\sqrt{(1+2l)(1+2m)(1+2n)}\,\tau_{ij(l,m,n)}^{\mathrm{T}(\alpha\beta\gamma)} P_l(\zeta_1^{(\alpha)})P_m(\zeta_2^{(\beta)})P_n(\zeta_3^{(\gamma)}), \tag{19}$$

where the non-dimensionalized variables $\zeta_i^{(\cdot)}$'s, defined in the interval $-1 \leqslant \zeta_i^{(\cdot)} \leqslant +1$, are given in terms of the local subcell coordinates as follows

$$\zeta_1^{(\alpha)} = \bar{x}_1^{(\alpha)}/(d_\alpha/2), \quad \zeta_2^{(\beta)} = \bar{x}_2^{(\beta)}/(h_\beta^{(q)}/2), \quad \zeta_3^{(\gamma)} = \bar{x}_3^{(\gamma)}/(l_\gamma^{(r)}/2).$$

The strain and thermal stress coefficients $e_{ij(l,m,n)}^{(\alpha\beta\gamma)}$, $\tau_{ij(l,m,n)}^{\mathrm{T}(\alpha\beta\gamma)}$ are explicitly determined in terms of the displacement and temperature field microvariables using orthogonal properties of Legendre polynomials. The stress coefficients $\tau_{ij(l,m,n)}^{(\alpha\beta\gamma)}$ are expressed in terms of the strain coefficients, the thermal stress coefficients and the unknown inelastic strain distributions, by first substituting the Legendre polynomial representations for $\boldsymbol{\varepsilon}^{(\alpha\beta\gamma)}$, $\boldsymbol{\sigma}^{(\alpha\beta\gamma)}$, and $\boldsymbol{\sigma}^{\mathrm{T}(\alpha\beta\gamma)}$ into the constitutive equations, and then utilizing the orthogonality of Legendre polynomials. This produces

$$\tau_{ij(l,m,n)}^{(\alpha\beta\gamma)} = [\lambda^{(\alpha\beta\gamma)}\delta_{ij}\delta_{kl} + \mu^{(\alpha\beta\gamma)}(\delta_{ik}\delta_{jl} + \delta_{il}\delta_{jk})]e_{kl(l,m,n)}^{(\alpha\beta\gamma)} - \tau_{ij(l,m,n)}^{\mathrm{T}(\alpha\beta\gamma)} - R_{ij(l,m,n)}^{(\alpha\beta\gamma)}, \tag{20}$$

where $R_{ij(l,m,n)}^{(\alpha\beta\gamma)}$ terms represent inelastic strain distributions calculated in the following manner,

$$R_{ij(l,m,n)}^{(\alpha\beta\gamma)} = \mu^{(\alpha\beta\gamma)}\Lambda_{(lmn)}\int_{-1}^{+1}\int_{-1}^{+1}\int_{-1}^{+1}\varepsilon_{ij}^{\mathrm{in}(\alpha\beta\gamma)}P_l(\zeta_1^{(\alpha)})P_m(\zeta_2^{(\beta)})P_n(\zeta_3^{(\gamma)})\mathrm{d}\zeta_1^{(\alpha)}\,\mathrm{d}\zeta_2^{(\beta)}\,\mathrm{d}\zeta_3^{(\gamma)}, \tag{21}$$

with

$$\Lambda_{(lmn)} = \frac{1}{4}\sqrt{(1+2l)(1+2m)(1+2n)}.$$

The upper limits on the summations in Eq. (18) are chosen so that an accurate representation of the stress field is obtained in each subcell, which depends on the extent of inelastic flow.

The microvariables $W_{i(lmn)}^{(\alpha\beta\gamma)}$ ($i = 1, 2, 3$) are determined from conditions similar to those employed in the thermal problem. In this case, there are 104 unknown microvariables in a generic cell (q,r), accounting for the periodicity in the x_1 direction and the use of a partial homogenization procedure along this direction. This procedure establishes a relationship between the constant term $W_{1(000)}^{(\alpha\beta\gamma)}$ in Eq. (14) and the uniform composite strain $\bar{\varepsilon}_{11}$ which enables analysis of functionally graded elements in the x_2–x_3 plane under the generalized plane strain condition in the x_1 direction upon imposing the requirement that the average composite stress $\bar{\sigma}_{11}$ be zero.

The determination of the microvariables $W_{i(lmn)}^{(\alpha\beta\gamma)}$ parallels that of the thermal problem. Here, the heat conduction equation is replaced by the equilibrium equations, Eq. (12), and the continuity of tractions and displacements at the various interfaces replaces the continuity of heat fluxes and temperature. Finally, the boundary conditions involve the appropriate mechanical quantities. In particular, in satisfying the equilibrium equations in a volume-average sense, use is made of the following volume-average stresses

$$S_{ij(l,m,n)}^{(\alpha\beta\gamma)} = \frac{1}{v_{(\alpha\beta\gamma)}^{(q,r)}} \int_{-d_\alpha/2}^{d_\alpha/2} \int_{-h_\beta^{(q)}/2}^{h_\beta^{(q)}/2} \int_{-l_\gamma^{(r)}/2}^{l_\gamma^{(r)}/2} (\bar{x}_1^{(\alpha)})^l (\bar{x}_2^{(\beta)})^m (\bar{x}_3^{(\gamma)})^n \sigma_{ij}^{(\alpha\beta\gamma)} \mathrm{d}\bar{x}_1^{(\alpha)} \mathrm{d}\bar{x}_2^{(\beta)} \mathrm{d}\bar{x}_3^{(\gamma)}, \tag{22}$$

where $S_{ij(0,0,0)}^{(\alpha\beta\gamma)}$ is the average value of the stress component $\sigma_{ij}^{(\alpha\beta\gamma)}$ in the subcell, whereas higher-order stresses are obtained for other values of l, m and n. Satisfaction of the equilibrium equations results in the following relations in terms of the above volume-averaged stresses

$$\left[S_{1j(1,0,0)}^{(\alpha\beta\gamma)}/d_\alpha^2 + S_{2j(0,1,0)}^{(\alpha\beta\gamma)}/h_\beta^2 + S_{3j(0,0,1)}^{(\alpha\beta\gamma)}/l_\gamma^2 \right]^{(q,r)} = 0, \tag{23}$$

which can be expressed in terms of the mechanical and thermal microvariables, and the integrals of the inelastic strain distributions $R_{ij(l,m,n)}^{(\alpha\beta\gamma)}$ using Eqs. (18), (20) and (22).

Subsequently, continuity of *both* the tractions and displacements is imposed in a surface-average sense at the interfaces separating adjacent subcells, as well as neighboring cells. For instance, the traction continuity at the interfaces separating adjacent subcells within the generic cell (q,r) in the x_2 direction is imposed as follows

$$\frac{1}{l_\gamma^{(r)}} \int_{-l_\gamma^{(r)}/2}^{l_\gamma^{(r)}/2} \left[\sigma_{2j}^{(\alpha 1\gamma)}(h_1^{(q)}/2, \bar{x}_3^{(\gamma)}) \right]^{(q,r)} \mathrm{d}\bar{x}_3^{(\gamma)} = \frac{1}{l_\gamma^{(r)}} \int_{-l_\gamma^{(r)}/2}^{l_\gamma^{(r)}/2} \left[\sigma_{2j}^{(\alpha 2\gamma)}(-h_2^{(q)}/2, \bar{x}_3^{(\gamma)}) \right]^{(q,r)} \mathrm{d}\bar{x}_3^{(\gamma)}, \tag{24}$$

with similar expressions for the traction continuity at the interfaces between adjacent generic cells. Satisfaction of the traction continuity in the remaining directions is carried out in the same manner. The resulting conditions are obtained in terms of the volume-averaged stresses $S_{ij(l,m,n)}^{(\alpha\beta\gamma)}$ of different orders, which are then expressed in terms of the microvariables $W_{i(lmn)}^{(\beta\gamma)}$, $T_{(lmn)}^{(\alpha\beta\gamma)}$ and the inelastic integrals $R_{ij(l,m,n)}^{(\alpha\beta\gamma)}$. For example, the above continuity condition can be shown to reduce to the following expression after some algebraic manipulations,

$$\left[-12S_{2j(0,1,0)}^{(\alpha 1\gamma)}/h_1 + S_{2j(0,0,0)}^{(\alpha 2\gamma)} - 6S_{2j(0,1,0)}^{(\alpha 2\gamma)}/h_2 \right]^{(q,r)} - \left[S_{2j(0,0,0)}^{(\alpha 2\gamma)} + 6S_{2j(0,1,0)}^{(\alpha 2\gamma)}/h_2 \right]^{(q-1,r)} = 0. \tag{25}$$

Alternatively, the imposition of displacement continuity in the same surface-averaged sense as above between adjacent subcells within each generic cell, as well as between adjacent generic cells, generates a system of equations expressed directly in terms of the microvariables $W_{i(lmn)}^{(\beta\gamma)}$.

Finally, the boundary conditions can be specified in terms of surface-averaged displacements, normal derivatives of these displacements, or tractions on the external surfaces of boundary subcells. For instance, for cells located on the boundaries defined by the indices $q = 1, N_q$, the surface-averaged traction boundary conditions are

$$\frac{1}{l_\gamma^{(r)}} \int_{-l_\gamma^{(r)}/2}^{l_\gamma^{(r)}/2} \left[\sigma_{2j}^{(\alpha 1\gamma)}(-h_1^{(1)}/2, \bar{x}_3^{(\gamma)}) \right]^{(1,r)} \mathrm{d}\bar{x}_3^{(\gamma)} = t_{\mathrm{bottom}}^{(r)}(x_3), \tag{26}$$

$$\frac{1}{l_\gamma^{(r)}}\int_{-l_\gamma^{(r)}/2}^{l_\gamma^{(r)}/2}\left[\sigma_{2j}^{(\alpha 2\gamma)}(h_2^{(N_q)},\bar{x}_3^{(\gamma)})\right]^{(N_q,r)}\mathrm{d}\bar{x}_3^{(\gamma)} = t_{\mathrm{top}}^{(r)}(x_3), \tag{27}$$

where $j = 2, 3$, and $t_{\mathrm{bottom}}^{(r)}(x_3)$, and $t_{\mathrm{top}}^{(r)}(x_3)$ are the piece-wise uniform applied surface tractions on the horizontal boundaries in the x_2–x_3 plane (see Fig. 1), with similar expressions for the remaining boundaries.

Application of the above equations and conditions in a volumetric and a surface-average sense, respectively, produces a system of $104N_qN_r$ algebraic equations in the unknown coefficients $W_{i(lmn)}^{(\alpha\beta\gamma)}$ which implicitly depend on the inelastic strain distributions. The final form of this system of equations is symbolically represented by

$$\mathbf{KU} = \mathbf{f} + \mathbf{g}, \tag{28}$$

where the structural stiffness matrix $\mathbf{K}$ contains information on the geometry and thermomechanical properties of the individual $(\alpha\beta\gamma)$ subcells within the cells comprising the heterogeneous material, the displacement coefficient vector $\mathbf{U}$ contains the unknown coefficients that describe the displacement field in each subcell, i.e.,

$$\mathbf{U} = [\mathbf{U}_{11}^{(111)},\ldots,\mathbf{U}_{N_qN_r}^{(222)}],$$

where

$$\mathbf{U}_{qr}^{(\alpha\beta\gamma)} = [W_{1(100)},\ldots,W_{3(002)}]_{qr}^{(\alpha\beta\gamma)}$$

and the thermomechanical force vector $\mathbf{f}$ contains information on the mechanical boundary conditions and the thermal loading effects generated by the applied temperature. In addition, the inelastic force vector $\mathbf{g}$ contains elements given in terms of the integrals of inelastic strain distributions that are represented by the coefficients $R_{ij(lm,n)}^{(\alpha\beta\gamma)}$. These integrals depend implicitly on the elements of the displacement coefficient vector $\mathbf{U}$, requiring an incremental solution of Eq. (28) at each point along the loading path. The incremental solution procedure depends on the choice of the constitutive model used to describe the inelastic response of the constitutive phases. In the present investigation, a power-law creep model was employed to model the inelastic response of the different TBC materials as explained in more detail in Section 3.2.

Similarities and differences between the higher-order theory and standard displacement-based finite-element formulations have been described recently by Bansal and Pindera (2003). An important advantage of the present approach is the simultaneous satisfaction of displacement and traction continuity conditions between the different subvolumes of the spatially variable microstructure. This facilitates the determination of thermally-induced stresses across the top/bond coat interface in the present application involving heterogeneous bond coats, which cannot be easily captured due to very localized and very steep gradients in the thickness direction.

We end this section by noting that the microstructural interaction within a graded material explicitly taken into account by the higher-order theory outlined above can also be modeled at the continuum level using a gradient elasticity approach. Paulino and co-workers, for instance, have adapted this approach in studying mode III crack

propagation in an elastic graded material, Paulino et al. (2003). In the authors' formulation, two characteristic length scales, associated with volumetric and surface strain energies, are employed to describe the size scale effect resulting from the underlying microstructure. Such an approach is an attractive alterative to the explicit microstructural-based theory employed herein, particularly when information on the characteristic length scales is obtained from micromechanical considerations. However, the incorporation of inelastic effects into such gradient theory would require numerical implementation when employed in the solution of a boundary-value problem of the type considered herein.

3. Investigated TBC systems

3.1. TBC system geometry and loading

A flat TBC system, shown in Fig. 2 with heterogeneous bond coat microstructure in the vicinity of the rough top/bond coat interface, is subjected to a spatially uniform thermal loading such that it remains in a generalized plane strain state in the horizontal and out-of-plane directions. The rough interface between the top and bond coats is modeled by a periodically-varying sine form located at the mean elevation of 630 μm from the substrate's bottom, with the wavelength of 25 μm and total (crest-to-trough) amplitude of 10 μm. These are representative values employed by previous investigators in modeling surface roughness of plasma-sprayed coatings.

Due to the periodic nature of the modeled TBC's geometry, the analysis of thermally-induced stress and inelastic strain fields is performed on the repeating cross-sectional element bounded by two vertical planes passing through the crest and trough of the sinusoidally-varying interface. The height of the cross-sectional element is 880 μm and its width is 12.5 μm, which is half of the rough interface's wavelength, Fig. 2. This element is discretized into 36×12 N_q and N_r generic cells, or 72×24 subcells, in a manner that approximates the geometry of the sinusiodally-varying interface with sufficient accuracy. Fig. 3 illustrates the employed volume

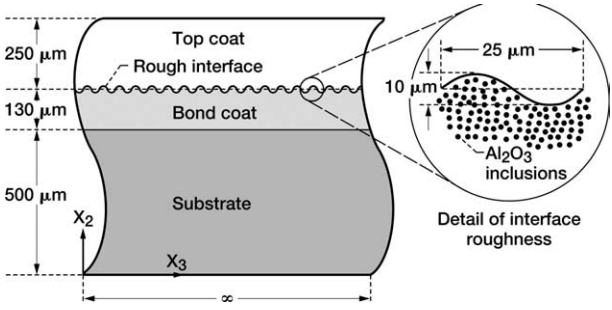

Fig. 2. A TBC system with a sinusoidally-varying top coat/bond coat interface and a heterogeneous bond coat in the interfacial region.

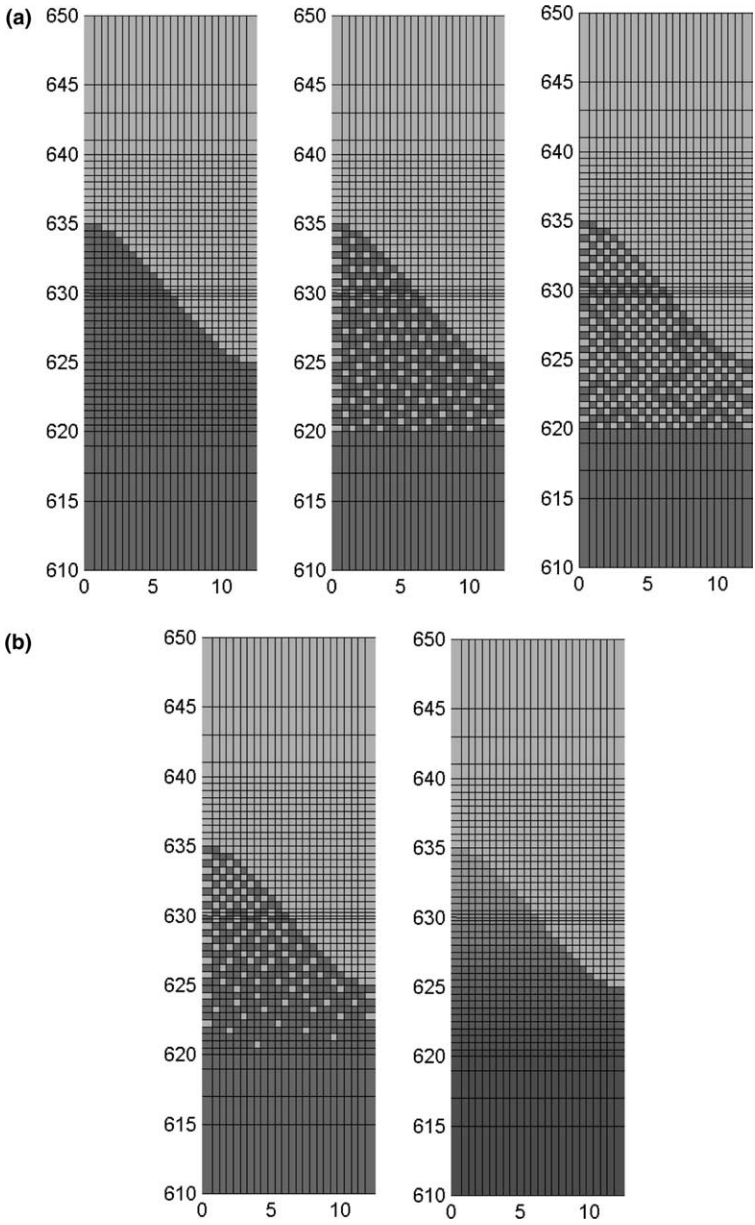

Fig. 3. Volume discretization of the sinusoidally-varying interface region showing TBCs with different types of bond coat (BC) microstructures (dimensions in μm, see Fig. 2). (a) Pure BC (left), 20% alumina BC (middle), 40% alumina BC (right). (b) BCs with actual (left) and homogenized (right) graded microstructures.

discretization in the region containing the wavy interface for the investigated TBCs where significant normal and shear stress components σ_{22} and σ_{23} develop due to the interfacial roughness. These stresses would not develop in the presence of a flat

interface. The stress and inelastic strain fields will be presented in this region in Section 4. As observed in the figure, the fine volume discretization of this region captures the sinusoidal interface with good fidelity, while ensuring that the stress gradients in the x_2 direction produced by the interfacial roughness are also captured with sufficient accuracy, as will be seen in Section 4. The finely discretized region bounded by the 620 and 640 μm elevations contains 42×24 subcells.

The discretized regions of the pure TBC system (consisting of the top coat, bond coat and substrate only), and heterogeneous bond coat TBC systems containing uniform dispersions of aluminum oxide (Al_2O_3) or alumina inclusions with 20% and 40% content in the vicinity of the top/bond coat interface within the bond coat, are shown in Fig. 3(a). The TBC systems with the actual and homogenized graded bond coat microstructures are shown in Fig. 3(b). The grading is accomplished by gradually decreasing the alumina particle content from 40% at the wavy interface's crest to 0% below the trough. The homogenized microstructure of the graded bond coat was obtained by dividing the region containing the actual microstructure into eight layers with progressively decreasing alumina particle content in increments of generally 5%, see Table 1. The average or macroscopic properties of each layer were then calculated using the Generalized Method of Cells micromechanics model, Aboudi (1995), to produce the layer-wise graded homogenized microstructure as discussed in the following section.

The employed spatially uniform thermal loading as a function of time is illustrated in Fig. 4. This loading history simulates furnace thermal cycling used in TBC durability testing by the aircraft industry. The temperature history is applied at each boundary subcell of the representative cross-sectional element. Under steady-state conditions employed in the present analysis (i.e. in the absence of transient effects), precisely the same temperature history is obtained within each interior subcell upon solving the thermal boundary value problem defined by Eq. (11). This temperature history then plays the role of a body force in the solution of the mechanical problem defined by Eq. (28).

In the solution of the mechanical problem, symmetry boundary conditions were imposed on the deformation of the representative cross-sectional element's vertical planes which are consistent with the modeled geometry and the generalized plane strain state (namely, $\bar{\sigma}_{11} = \bar{\sigma}_{33} = 0$, where the bars denote average values of the

Table 1
Geometric details of the eight layer-wise homogenized NiCrAlY + Al_2O_3 region

Layer number	Vertical location (μm)	β subcell number	Al_2O_3 content (%)
1	$635 \rightarrow 632$	$47 \rightarrow 42$	40
2	$632 \rightarrow 629\frac{1}{2}$	$41 \rightarrow 35$	35
3	$629\frac{1}{2} \rightarrow 628$	$34 \rightarrow 32$	30
4	$628 \rightarrow 626\frac{1}{2}$	$31 \rightarrow 29$	25
5	$626\frac{1}{2} \rightarrow 625$	$28 \rightarrow 26$	20
6	$625 \rightarrow 623\frac{1}{2}$	$25 \rightarrow 23$	15
7	$623\frac{1}{2} \rightarrow 622$	$22 \rightarrow 20$	11
8	$622 \rightarrow 620\frac{1}{2}$	$19 \rightarrow 17$	6

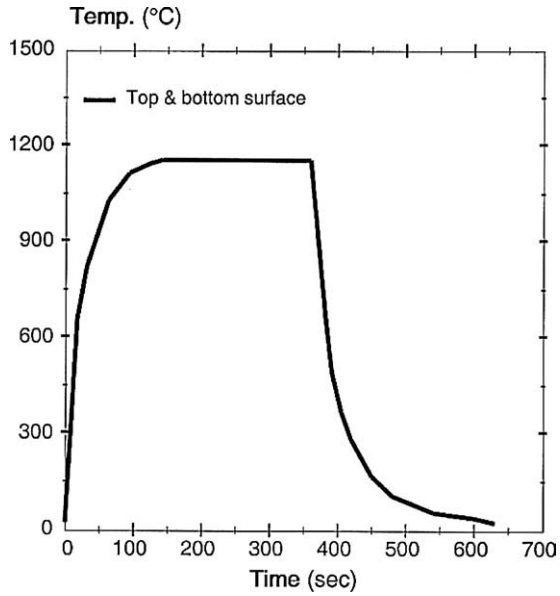

Fig. 4. Thermal loading history applied to the boundary subcells of the TBC cross-sectional representative element (see Fig. 3).

normal stresses in the x_2–x_3 and x_1–x_2 planes). That is, the left vertical plane of the representative cross-sectional element is constrained from rotation and motion along the x_3 axis by imposing the following conditions on the external surfaces of the boundary cells $(q,1)$

$$\frac{1}{h_\beta^{(q)}}\int_{-h_\beta^{(q)}/2}^{h_\beta^{(q)}/2}\left[u_3^{(\alpha\beta 1)}(\bar{x}_2^{(\beta)},-l_1^{(1)}/2)\right]^{(q,1)}\mathrm{d}\bar{x}_2^{(\beta)}=0, \tag{29}$$

$$\frac{1}{h_\beta^{(q)}}\int_{-h_\beta^{(q)}/2}^{h_\beta^{(q)}/2}\frac{\partial}{\partial\bar{x}_3^{(1)}}\left[u_2^{(\alpha\beta 1)}(\bar{x}_2^{(\beta)},\bar{x}_3^{(1)})\right]_{-l_1^{(1)}/2}^{(q,1)}\mathrm{d}\bar{x}_2^{(\beta)}=0. \tag{30}$$

Similarly, the right vertical plane is constrained from rotation, but allowed to translate uniformly along the x_3 axis by the amount $\bar{\varepsilon}_{33}L$ such that $\bar{\sigma}_{33}=0$. Therefore, the following conditions are imposed on the external surfaces of the boundary cells $(q,\ N_r)$

$$\frac{1}{h_\beta^{(q)}}\int_{-h_\beta^{(q)}/2}^{h_\beta^{(q)}/2}\left[u_3^{(\alpha\beta 2)}(\bar{x}_2^{(\beta)},l_2^{(N_r)}/2)\right]^{(q,N_r)}\mathrm{d}\bar{x}_2^{(\beta)}=\bar{\varepsilon}_{33}L, \tag{31}$$

$$\frac{1}{h_\beta^{(q)}}\int_{-h_\beta^{(q)}/2}^{h_\beta^{(q)}/2}\frac{\partial}{\partial\bar{x}_3^{(2)}}\left[u_2^{(\alpha\beta 2)}(\bar{x}_2^{(\beta)},\bar{x}_3^{(2)})\right]_{l_2^{(N_r)}/2}^{(q,N_r)}\mathrm{d}\bar{x}_2^{(\beta)}=0, \tag{32}$$

where $L = 12.5$ μm. Further, the bottom horizontal boundary is constrained from motion in the vertical direction by imposing the following conditions on the external surfaces of the boundary cells (1,r)

$$\frac{1}{l_\gamma^{(r)}}\int_{-l_\gamma^{(r)}/2}^{l_\gamma^{(r)}/2}\left[u_2^{(\alpha 1\gamma)}(-h_1^{(1)}/2,\bar{x}_3^{(\gamma)})\right]^{(1,r)}\mathrm{d}\bar{x}_3^{(\gamma)} = 0, \tag{33}$$

$$\frac{1}{l_\gamma^{(r)}}\int_{-l_\gamma^{(r)}/2}^{l_\gamma^{(r)}/2}\frac{\partial}{\partial \bar{x}_2^{(1)}}\left[u_3^{(\alpha 1\gamma)}(\bar{x}_2^{(1)},\bar{x}_3^{(\gamma)})\right]_{-h_1^{(1)}/2}^{(1,r)}\mathrm{d}\bar{x}_3^{(\gamma)} = 0, \tag{34}$$

while the top boundary is traction-free, i.e.,

$$\frac{1}{l_\gamma^{(r)}}\int_{-l_\gamma^{(r)}/2}^{l_\gamma^{(r)}/2}\left[\sigma_{2j}^{(\alpha 2\gamma)}(h_2^{(N_q)}/2,\bar{x}_3^{(\gamma)})\right]^{(N_q,r)}\mathrm{d}\bar{x}_3^{(\gamma)} = 0, \tag{35}$$

where $j = 2, 3$.

3.2. Constituents' material response

The material thermoelastic and viscoplastic parameters that govern the response of the individual TBC constituents are given in Table 2. These are the same as the parameters used in our previous investigation dealing with the effects of interfacial roughness and oxide film thickness on the inelastic response of TBCs with homogeneous bond coats, Pindera et al. (2000), and are based on the properties employed by Freborg et al. (1998). The viscoplastic response of the zirconia top coat, NiCr-based bond coat, and Ni-based substrate is modeled by a power-law creep equation, generalized to multi-axial loading situations as follows,

$$\dot{\varepsilon}_{ij}^{c} = \frac{3F(\sigma_e,T)}{2\sigma_e}\sigma'_{ij}, \tag{36}$$

where σ'_{ij} are the components of the stress deviator, $\sigma_e = \sqrt{3/2\sigma'_{ij}\sigma'_{ij}}$, and

$$F(\sigma_e,T) = A(T)\sigma_e^{n(T)}, \tag{37}$$

where the temperature-dependent parameters A, n are listed in the table in the range 10–1200° C (see Pindera et al. (2003) for details). This particular inelastic model was employed because the investigated mechanism is dominated by creep/relaxation ef-

Table 2
Thermoelastic and creep material parameters of the TBC constituents (see Pindera et al. (2003) for details)

Material	E (GPa)	ν	α (10^{-6}/°C) 10 → 1200 °C	A (MPa^{-n}/s) 10 → 1200 °C	n 10 → 1200 °C
Zr-based top coat	25.4	0.33	7.6 → 12.5	$2.01\times10^{-30} \rightarrow 1.85\times10^{-7}$	1.0 → 3.0
Al_3O_2 inclusions	380	0.26	8.6	–	–
NiCrAlY bond coat	156	0.27	12.0 → 14.4	$4.39\times10^{-40} \rightarrow 7.40\times10^{-6}$	1.0 → 3.0
Ni substrate	156	0.27	12.0 → 19.3	$4.85\times10^{-36} \rightarrow 2.25\times10^{-9}$	1.0 → 3.0

fects occurring during exposure to the high temperatures considered herein. The results generated using this model, for which the material parameters are available, can therefore be compared to those reported in the literature.

The alumina particles are assumed to be elastic since their creep response is small for the employed thermal loading compared with the other materials. Further, the pronounced inelastic response of plasma-sprayed zirconia compared to fully densified zirconia is due to the local deformation mechanisms activated by porosities and microcracks introduced during the plasma-sprayed process, as discussed by DiMassi-Marcin et al. (1990). These microstructural details are not explicitly taken into account in the present analysis. The power-law creep model for the inelastic response of zirconia has been shown to model the overall average or macroscopic effect of these mechanisms with sufficient accuracy.

In the analysis based on the actual TBC microstructures shown in Fig. 3, the inelastic strain increment $d\varepsilon_{ij}^{in(\alpha\beta\gamma)}$ within the subcells containing different materials was calculated by integrating Eq. (36) using the parameters shown in Table 2 for the material occupying the particular subcell. This strain increment was then used to update the inelastic strain field at a number of points within the subcell, which also determines the total stress field given by Eq. (13), in the incremental solution procedure of the global system of equations governing the microvariable evolution, Eq. (28). A forward Euler method with an adjustable time step was used in updating the various field quantities at each time increment of the applied thermal history.

The analysis based on the homogenized properties of the NiCrAlY + Al_2O_3 graded region shown in the right portion of Fig. 3(b) also employs the same volume dicretization as the analysis based on the actual TBC microstructure. In this case, however, the subcells in each of the eight homogenized layers into which the graded region was divided contain the same material with homogenized properties which depend on the content of the Al_2O_3 inclusions. In the case of elastic analysis, the homogenization of the local microstructure can be performed a priori using the chosen micromechanics model to generate macroscopic properties that are subsequently used in the global or structural analysis. When inelastic effects are present whose evolution depends on the loading history, however, two approaches present themselves. The more rigorous approach dictates that the homogenization procedure be embedded directly into the global analysis to determine the local history-dependent homogenized material response at each point for use in the global analysis "on the fly". This approach was employed by Pindera et al. (1994) to analyze the response of a unidirectional metal matrix composite with a functionally graded interface under axisymmetric thermal loading which produced radially-dependent displacement field. In the presence of two-dimensional dependence of the field variables, however, this approach becomes computationally demanding. In the present case, therefore, the macroscopic elastic properties of the homogenized layers as well as the macroscopic form of the power-law creep model were determined a priori for use in the global analysis of the representative cross-sectional elements of the investigated TBCs as described below. A similar approach was employed by Kim and Paulino (2003) in the context of an elastic two-dimensional finite-element analysis of cracks in functionally graded

materials using the self-consistent, Mori–Tanaka and three-phase micromechanical models.

In the present investigation, the Generalized Method of Cells micromechanics model was employed to calculate the macroscopic thermoelastic and creep parameters of the eight homogenized layers in the graded region. This micromechanics model has been shown to predict with sufficient accuracy the macroscopic or homogenized elastic as well as inelastic response of two-phase composites despite the fact that the local fields are not as accurately captured (cf. Aboudi et al., 2003). The homogenized Young's moduli, Poisson's ratios, and thermal expansion coefficients as a function of the alumina inclusion content in the range 10–1200 °C are given in Table 3. Fig. 5 illustrates graphically the reduction of the top/bond coat thermal expansion coefficient mismatch as a function of temperature for different alumina particle content in the homogenized bond coat layers relative to the pure top coat zirconia and bond coat NiCrAlY constituents. As mentioned previously, this mismatch is considered to be important in controlling the evolution of residual stresses in TBCs. As observed, appreciable reduction in the thermal expansion mismatch is attained for bond coat alumina content greater than twenty percent.

In order to determine the macroscopic creep response of the homogenized layers, creep experiments were simulated for different volume fractions of the Al_2O_3 inclusions in the NiCrAlY matrix at different temperatures as follows. A very rapid rate of uniaxial loading up to a pre-determined load level was applied to the representative volume element for the particular NiCrAlY + Al_2O_3 microstructure, and then that load was held constant for a fixed period of time. The resulting macroscopic strain predicted by the Generalized Method of Cells at different times was then used to determine the functional form of the macroscopic creep model. These numerical simulations, or experiments, revealed that the creep response of the homogenized layers exhibits very little primary creep, with the macroscopic strain rate quickly becoming constant over the period of numerical simulations, which was chosen to be on the order of the employed thermal loading history shown in Fig. 4. That is, the functional form of the multi-axial creep model for the homogenized layers remained the same as that of the pure NiCrAlY matrix given by Eqs. (36) and (37), with the creep parameters A and n modified by the Al_2O_3 inclusion presence as follows

$$A(T) \rightarrow A^*(T, c_{Al_2O_3}) \qquad n(T) \rightarrow n^*(T, c_{Al_2O_3}). \tag{38}$$

Table 3
Homogenized thermoelastic moduli and power-law creep parameters of the heterogeneous bond coat as a function of the alumina inclusion concentration $c_{Al_2O_3}$ (by volume) and temperature (see Pindera et al. (2003) for details)

$c_{Al_2O_3}$	E^* (GPa)	ν^*	α^* (10^{-6}/°C) 10 → 1200 °C	A^* (MPa^{-n}/s) 10 → 1200 °C	n^* 10 → 1200 °C
10%	169.9	0.266	11.54 → 13.67	$3.59\times10^{-40} \rightarrow 5.11\times10^{-6}$	1.0 → 3.0
20%	187.1	0.262	11.08 → 12.92	$2.94\times10^{-40} \rightarrow 3.24\times10^{-6}$	1.0 → 3.0
30%	206.7	0.258	10.62 → 12.19	$2.33\times10^{-40} \rightarrow 1.87\times10^{-6}$	1.0 → 3.0
40%	228.5	0.254	10.18 → 11.49	$1.71\times10^{-40} \rightarrow 5.02\times10^{-7}$	1.0 → 3.0

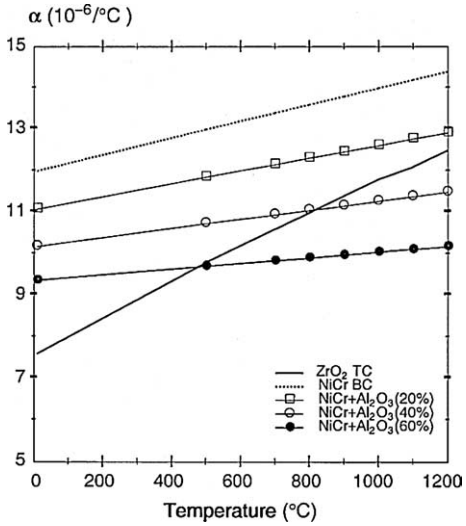

Fig. 5. Thermal expansion coefficient vs temperature of pure zirconia, and pure and heterogeneous NiCrAlY bond coat material with different alumina particle content.

These parameters depend on the alumina particle concentration $c_{Al_2O_3}$ at different temperatures and are included in Table 3 (see Pindera et al. (2003) for details). Examination of the data reveals that of the two creep parameters in the power-law creep model for the homogenized NiCrAlY + Al_2O_3 layers, the power-law creep coefficient is the parameter most affected by the Al_2O_3 inclusion presence, with the power-law creep exponent remaining generally unaffected by the microstructural effects for this particular material system in the given Al_2O_3 volume fraction range.

The above numerical results which indicate that the functional form of the power-law creep response at the constituent level retains the same form at the homogenized composite level, although somewhat surprising, is not new. This finding for our material system is consistent with the results reported by Crossman et al. (1974) and Crossman and Karlak (1976) in the context of the creep response of metal matrix composites.

4. Numerical results

In this communication, we focus on the two stress components in the vicinity of the wavy interface in the x_2–x_3 plane that have the potential to influence the initiation (and subsequent growth) of local horizontal cracks in the top coat, namely the normal stress σ_{22} and the shear stress σ_{23}. The influence of the normal stress σ_{22} on top coat delamination leading to spallation has been extensively investigated for pure TBCs with evolving oxide film. The role that the inplane shear stress may play in the delamination process in the presence of a horizontal crack above the wavy interface, on the other hand, has only recently been discussed by Pindera et al. (2003). The

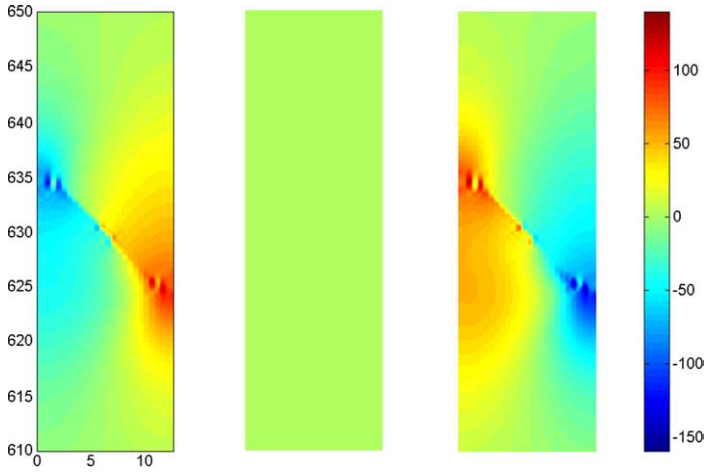

(a) σ_{22} distributions at 30 (left), 360 (middle), 630 (right) seconds.

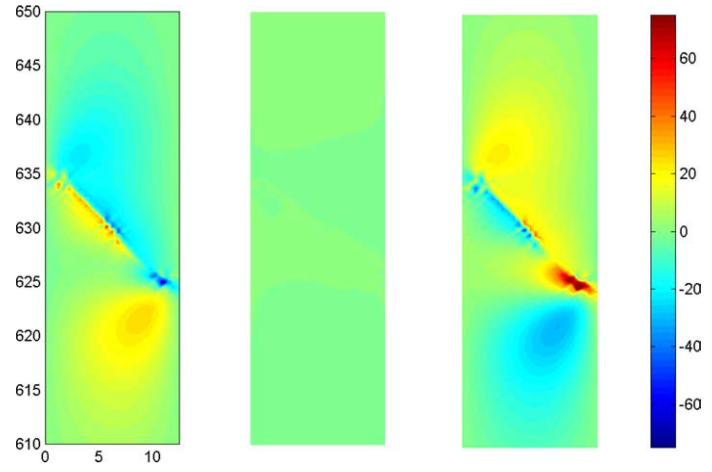

(b) σ_{23} distributions at 30 (left), 360 (middle), and 630 (right) seconds.

Fig. 6. Evolution of σ_{22} (a) and σ_{23} (b) stress distributions with time in the interfacial region of a pure TBC during the first thermal cycle (colorbar scale in MPa).

region of interest is the top coat just above the wavy interface where horizontal cracks are generally assumed to initiate.

In addition, two measures of inelastic strain accumulation during thermal cycling are included in the results as they may provide important information useful in fatigue life calculations. The integrated effective inelastic strain measure is defined in the standard way as

$$\varepsilon_{\text{eff}}^{\text{int}} = \int \mathrm{d}\varepsilon_{\text{eff}}^{\text{c}}, \tag{39}$$

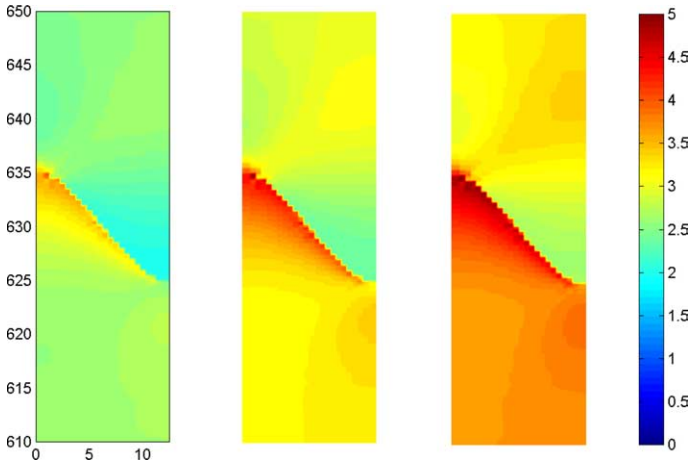

(c) $\varepsilon_{\text{eff}}^{\text{int}}$ distributions at 1290 (left), 1620 (middle), and 1890 (right) seconds.

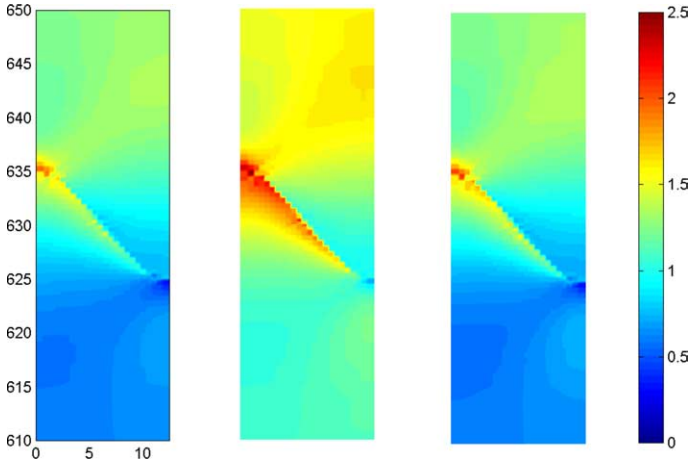

(d) $\varepsilon_{\text{eff}}^{\text{res}}$ distributions at 1290 (left), 1620 (middle), and 1890 (right) seconds.

Fig. 6. *(continued)* Evolution of $\varepsilon_{\text{eff}}^{\text{int}}$, (c) and $\varepsilon_{\text{eff}}^{\text{res}}$ (d) inelastic strain distributions with time in the interfacial region of a pure TBC during the third thermal cycle (colorbar scale in % strain).

where $\mathrm{d}\varepsilon_{\text{eff}}^{\text{c}} = \sqrt{2/3\mathrm{d}\varepsilon_{ij}^{\text{c}}\mathrm{d}\varepsilon_{ij}^{\text{c}}}$. It is always positive and cannot decrease. In the presence of cyclic loading where inelastic strain reversal occurs, this measure represents the total inelastic strain history that a material experiences at a given point. It will increase monotonically during the evolution of inelastic strain even when inelastic strain reversal occurs due to the way it has been defined, tending asymptotically to a certain limit in those situations when the inelastic strain growth tends to zero. In order to ascertain the possibility of inelastic strain reversal, the residual inelastic effective strain measure is defined in terms of the total creep strain components $\varepsilon_{ij}^{\text{c}}$

$$\varepsilon_{\text{eff}}^{\text{res}} = \sqrt{2/3[(\varepsilon_{11}^{\text{c}})^2 + (\varepsilon_{22}^{\text{c}})^2 + (\varepsilon_{22}^{\text{c}})^2 + 2(\varepsilon_{23}^{\text{c}})^2 + 2(\varepsilon_{12}^{\text{c}})^2 + 2(\varepsilon_{13}^{\text{c}})^2]}. \tag{40}$$

This measure yields the instantaneous value of the effective inelastic strain, and upon comparison with the integrated measure, provides information on the inelastic strain reversal. Clearly, the two measures will produce the same value when the inelastic strain components increase or decrease monotonically and proportionally. During non-proportional and non-monotonic inelastic strain evolution, the two values generally will be different. In particular, when inelastic strain reversal occurs during cyclic loading, $\varepsilon_{\text{eff}}^{\text{int}}$ will be greater than $\varepsilon_{\text{eff}}^{\text{res}}$, with the difference providing a measure of inelastic strain reversal.

4.1. Baseline results for a homogeneous TBC

As the first step, we establish baseline results for the response of a pure TBC system subjected to the thermal cycle illustrated in Fig. 4 applied successively three times. Fig. 6 illustrates the evolution of the two stress components during the first cycle at t = 30, 360, and 630 s, Figs. 6(a) and (b), and the two measures of the effective inelastic strain during the third cycle at t = 1290, 1620, and 1890 s, Figs. 6(d) and (e). These times correspond to points along the thermal history during the initial heating period, end of the hold period, and end of the entire cycle. During the first cycle, the normal stress σ_{22} attains maximum and minimum values at the crest and trough of the wavy interface at these times.

The normal stress σ_{22} distributions in the vicinity of the wavy interface (in the same region as shown in Fig. 3) at the three times are shown in Fig. 6(a). During the initial heating period in the first cycle, the normal stress σ_{22} is compressive in the crest region and tensile in the trough region. This stress component relaxes to nearly zero during the hold period of the thermal cycle, thereby becoming tensile in the crest region and compressive in the trough region upon cooldown. This is consistent with the previously reported results discussed earlier. During subsequent cycles, the σ_{22} distribution decreases upon heatup, relaxes to nearly zero during the hold period, and returns to essentially the same state upon cooldown as that at the end of the first cycle, Pindera et al. (2003). The maximum magnitudes occur in the crest and trough regions.

Similar relaxation effects are observed in the distributions of the shear stress σ_{23} component, Fig. 6(b). In this case, the stress distributions are characterized by a sign change across the wavy interface and the maximum stress magnitudes occur somewhat off the crest and trough locations. During the initial heatup period in the first cycle, the shear stress changes from positive to negative as the interface is traversed from the bond coat to the top coat regions almost along the entire interface. Stress relaxation during the hold period produces a sign reversal in the top coat shear stress along the entire interface upon cooldown. As in the case of the normal stress, during subsequent cycles the shear stress decreases during the heatup stage and returns to the state attained after completion of the first cycle upon cooldown.

The two measures of the effective inelastic strain distributions are shown in Figs. 6(c) and (d) during the third cycle at $t = 1290$, 1620, and 1890 s. These times correspond to the same points in the thermal cycle as the times at which the stress distributions during the first cycle were shown. Results from the third rather than the first cycle are shown because the difference in the two inelastic strain measures increases with the number of accumulated cycles. In the case of the integrated strain measure, Fig. 6(c), we observe continuous inelastic strain growth which initiates at the wavy interface's crest during the first cycle and eventually spreads to the bond coat in subsequent cycles, with the maximum magnitudes occurring along the wavy interface on the bond coat side. The distributions of the residual effective inelastic strain, Fig. 6(d), indicate that substantial inelastic strain accumulation occurs during the time up to the end of the hold period and then actually decreases upon cooldown, with the maximum magnitude of this strain measure occurring at the wavy interface's crest. The same behavior is observed during the first cycle, albeit with smaller magnitudes and differences between the two effective inelastic strain measures. A small increase in the residual effective inelastic strain is observed at the wavy interface's crest at the end of the third cycle relative to the first cycle. These results indicate that inelastic strain reversal occurs during thermal cycling which could potentially produce fatigue-like failures in the porous top coat due to repeated relative sliding of the microcrack faces.

4.2. Effect of spatially uniform bond coat microstructure

The experimental results of Brindley et al. (1998) suggest that reduction of the top/bond coat thermal expansion mismatch may potentially improve TBC durability. In this section, we examine the effect of a uniform dispersion of alumina inclusions in the vicinity of the wavy interface on the normal and shear stress components in the x_2–x_3 plane and the two effective inelastic strain measures. Fig. 5 indicates that a relatively large alumina inclusion content is required to attain an appreciable reduction in the top/bond coat thermal expansion mismatch, which is substantially greater than the 5% and even 20% alumina particle content employed by Brindley and co-workers. This suggests that another mechanism may have been operative that improved the investigated TBCs' durability. Nevertheless, we employ 20% and 40% volume fractions of the alumina particles in the NiCrAlY matrix in the interfacial region to investigate the thus-far unquantified effect of the thermal expansion mismatch reduction through the use of heterogeneous bond coats on the evolution of stress and inelastic strain fields in the considered model TBC system.

In view of the stress field's stabilization after cooldown with subsequent cycles demonstrated previously by Pindera et al. (2003), the results are presented at $t = 630$ s, or at the end of the first cycle. The field quantities were generated in two distinct ways that reflect the present dichotomy of modeling microstructural effects in heterogeneous materials. First, the bond coat microstructure was homogenized in the manner described earlier, and the homogenized effective properties were employed in the analysis. Subsequently, the analysis was repeated with the actual bond coat microstructure explicitly taken into account.

Fig. 7(a) compares the effect of alumina inclusion content on the normal σ_{22} stress distributions. The stress distribution in a TBC with homogeneous bond coat is included for convenient reference. The results indicate that when the actual bond coat microstructure is homogenized (top portion of Fig. 7(a)), reduction in the normal stress at the crest of the wavy interface is achieved which increases with increasing alumina inclusion content. At 40% of the alumina volume content, the reduction in the normal stress at the wavy interface's crest is substantial. This, however, is obtained at the expense of an increase in the magnitude and size of the compressive normal stress field at the interface's trough, as well as increased magnitude of the normal stress in the bond coat below the interface's crest. Alternatively, when the analysis is based on the actual bond coat microstructure, the extent of the normal stress reduction at the wavy interface's crest is quite modest (bottom portion of Fig. 7(a)), and the normal stress distributions in the heterogeneous region are qualitatively and quantitatively different from their homogenized counterparts.

Fig. 7(b) illustrates that the effect of alumina content on the shear stress distribution is *in principle* similar to that observed in the case of the normal stress σ_{22}. That is, increasing the alumina content decreases the shear stress in the top coat's crest region and increases it in the bond coat's trough region. However, the significant difference in this case is the change of the shear stress sign in the crest region with increasing alumina content. This results in an increase of the shear stress *magnitude* with increasing alumina content. In the trough region, the sign of the shear stress is not affected. The analysis based on the homogenized bond coat properties tends to underestimate the increase in the shear stress magnitude on the top coat side of the interface relative to the analysis based on the actual bond coat microstructure. However, the extent of the spread of the shear stress into the trough region is overestimated.

The effect of bond coat microstructure on the integrated effective inelastic strain is demonstrated in Fig. 7(c). The homogenized analysis predicts a decrease in this inelastic strain measure with increasing alumina content directly at the wavy interface's crest on both sides of the interface relative to the homogeneous bond coat results. Also, continuous increase is observed in the trough region of the top coat with increasing alumina content. In the bond coat itself, the growth of the integrated effective inelastic strain is suppressed directly below the crest of the wavy interface and shifts further down into the bond coat region with increasing alumina content. In contrast, the analysis based on the actual bond coat microstructure indicates that the integrated effective inelastic strain actually increases directly at the interface's crest where horizontal cracks initiate. In addition, substantially smaller values of this inelastic strain measure are predicted in the top coat's trough region relative to the homogenized analysis. Further, channeling effects are observed in the bond coat itself, where distinct paths of intensive inelastic strain localization are observed. Similar effects are observed in the case of the residual effective inelastic strain distributions, Fig. 7(d), with the differences between the two types of analysis somewhat magnified in the crest region of the top coat. Such effects are discussed in detail by Ostoja-Starzewski (in this issue) in the context of plasticity of random media resembling the investigated bond coat microstructures.

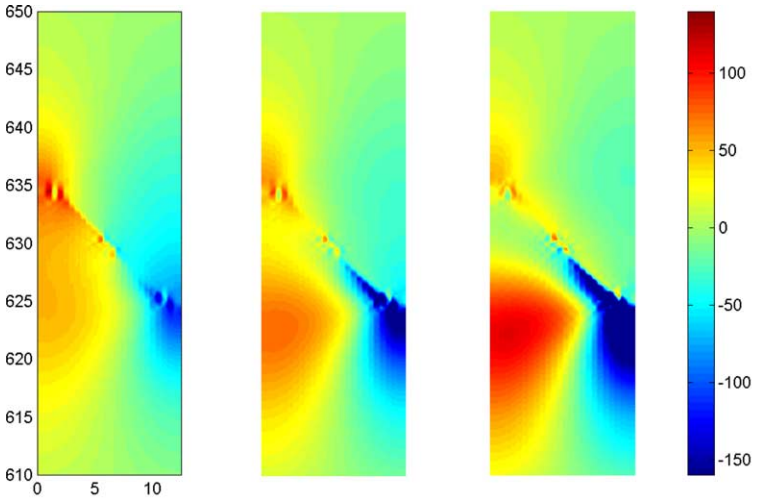

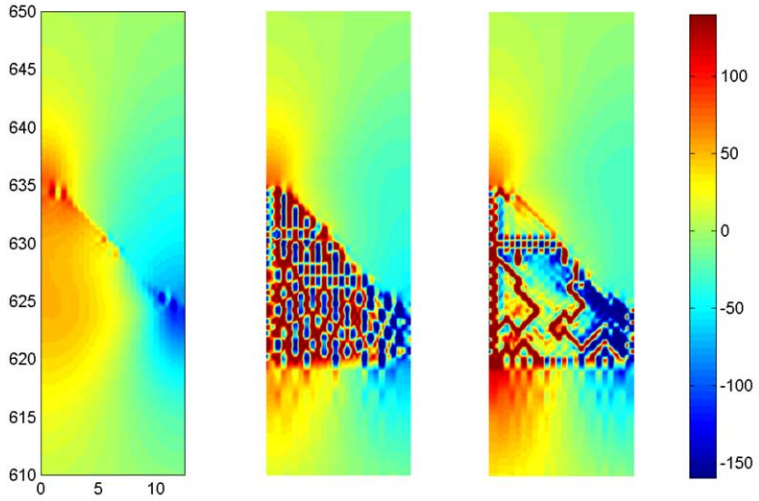

Fig 7. (a) Normal stress σ_{22} distributions in the interfacial region of a spatially uniform heterogeneous bond coat TBC with homogenized (top) and actual (bottom) microstructures at the end of the first thermal cycle, illustrating the alumina particle content influence (colorbar scale in MPa).

4.3. Effect of graded bond coat microstructure

The results of the preceding section indicate that the potentially beneficial effect of spatially uniform heterogeneous bond coat microstructure on the normal σ_{22} stress distribution in the top coat at the wavy interface's crest is offset by increased magnitude of this stress component in the trough region. Further, high alumina inclusion

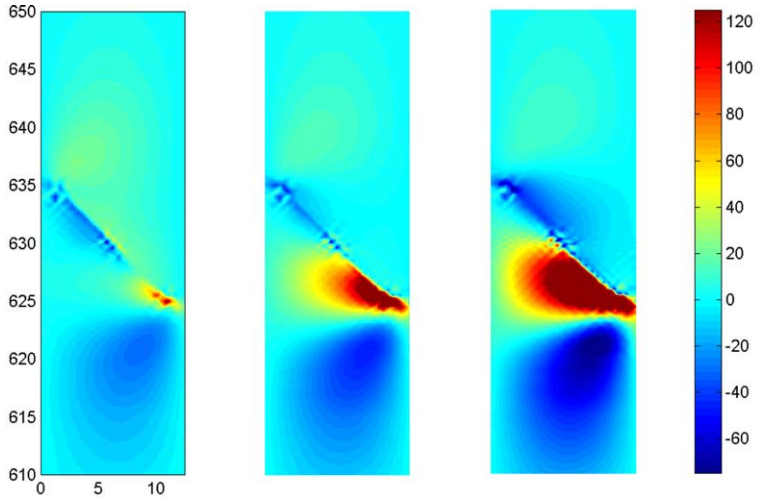

Homogeneous BC (left), 20% alumina BC (middle), 40% alumina BC (right)

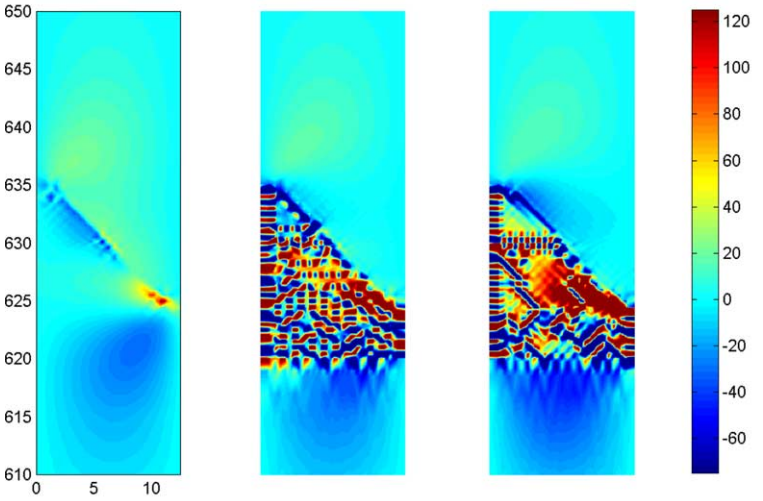

(b) Homogeneous BC (left), 20% alumina BC (middle), 40% alumina BC (right)

Fig 7. *(continued)* (b) Shear stress σ_{23} distributions in the interfacial region of a spatially uniform heterogeneous bond coat TBC with homogenized (top) and actual (bottom) microstructures at the end of the first thermal cycle, illustrating the alumina particle content influence (colorbar scale in MPa).

content produces large normal and shear stresses, and highly localized inelastic effective strain, in the bond coat itself. This suggests that these quantities can be managed in the affected regions by grading the bond coat microstructure from a high content in the crest region to a low content in the trough region. The effect of such grading strategy on the normal and shear stress and effective inelastic strain components is discussed in this section.

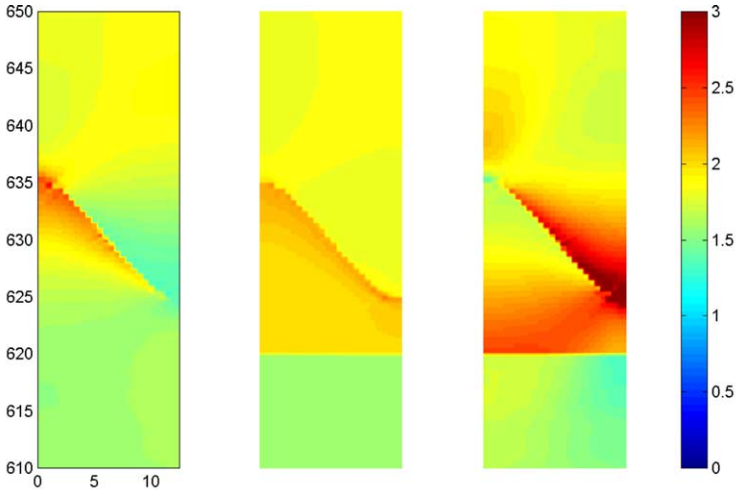

Homogeneous BC (left), 20% alumina BC (middle), 40% alumina BC (right)

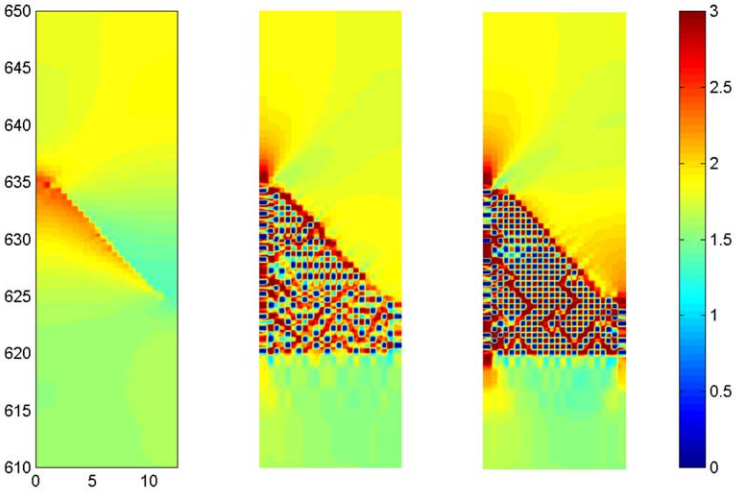

(c) Homogeneous BC (left), 20% alumina BC (middle), 40% alumina BC (right)

Fig 7. *(continued)* (c) Inelastic strain $\varepsilon_{\text{eff}}^{\text{int}}$ distributions in the interfacial region of a spatially uniform heterogeneous bond coat TBC with homogenized (top) and actual (bottom) microstructures at the end of the first thermal cycle, illustrating the alumina particle content influence (colorbar scale in % strain).

Fig. 8(a) illustrates the effect of grading on the normal stress σ_{22} distributions at the end of the first thermal cycle. It is observed that the normal stress at the crest of the wavy interface is very nearly the same as for the spatially uniform bond coat microstructures discussed earlier, while the magnitude of this stress component in the lower regions of the bond coat, including the trough region, is reduced. As in the previous cases, the analysis based on the homogenized bond coat microstructure

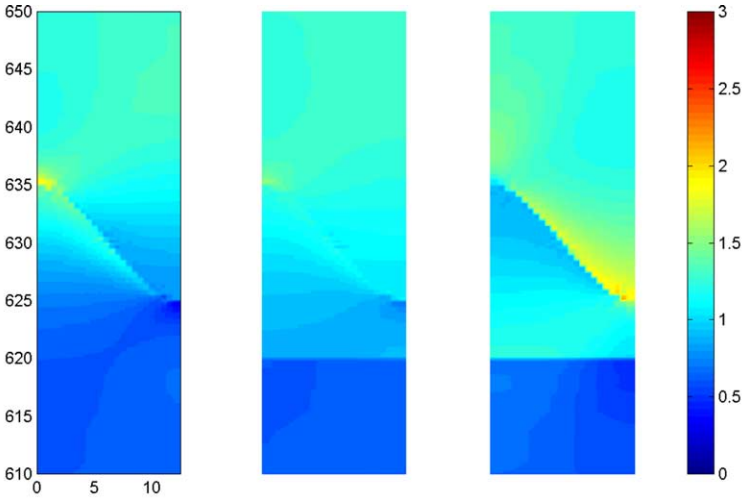

Homogeneous BC (left), 20% alumina BC (middle), 40% alumina BC (right)

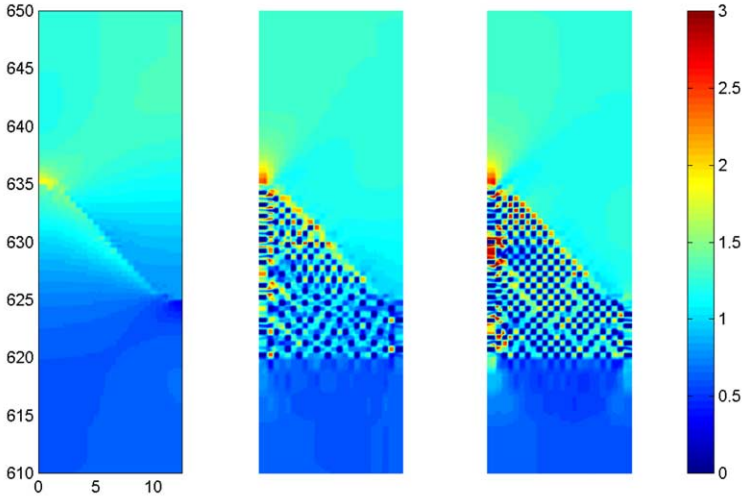

(d) Homogeneous BC (left), 20% alumina BC (middle), 40% alumina BC (right)

Fig. 7. *(continued)* (d) Inelastic strain $\varepsilon_{\text{eff}}^{\text{res}}$ distributions in the interfacial region of a spatially uniform heterogeneous bond coat TBC with homogenized (top) and actual (bottom) microstructures at the end of the first thermal cycle, illustrating the alumina particle content influence (colorbar scale in % strain).

overestimates the normal stress reduction at the wavy interface's crest, and the normal stress increase in the trough, relative to the analysis based on the actual bond coat microstructure.

Grading does reduce the magnitude of the shear stress σ_{23} in the bond coat's trough region, relative to the spatially uniform bond coat microstructure result, without affecting the shear stress in the top coat's crest region. As expected, the

greatest differences in the shear stress distributions predicted by the two types of analysis are observed in the heterogeneous bond coat where the highly localized and dispersed areas of positive and negative shear stress are not well captured by the analysis based on the homogenized bond coat microstructure.

Grading suppresses the evolution of the integrated effective inelastic strain in the trough region of the top coat, Fig. 8(c), relative to the spatially uniform bond coat microstructure, Fig. 7(c). This is also observed at the wavy interface's crest region in the top coat, and also within the bond coat, according to the analysis based on the homogenized bond coat properties, in contrast with the analysis based on the actual microstructure where little change is seen in the top coat at the crest. Similar observations hold in the case of the residual effective inelastic strain, Fig. 8(d), whose magnitude in the affected regions is now much smaller as in the previously discussed cases. The primary difference between the integrated and residual effective inelastic strain distributions lies in the bond coat, where the differences between the two types of analysis are now more pronounced in the integrated strain measure case due to the lower magnitudes of the residual effective inelastic strain.

5. Summary of results and discussion

The focus of previous investigations dealing with the evolution of stress fields in plasma-sprayed TBCs was on the stress component normal to the crest of the wavy top/bond coat interface. This stress component was hypothesized to play a major role in the spallation mechanism observed in this type of TBCs through the initiation of local horizontal cracks just above the rough interface's crest. These cracks were hypothesized to be subsequently driven by an evolving oxide film on the bond coat side of the interface, which altered the distribution of the normal stress ahead of the crack tip in the top coat's trough region. Since the thermal expansion mismatch between the bond and top coats is a major parameter in controlling the magnitude of the stress component normal to the interface, reducing this mismatch through the use of two-phase bond coats had been proposed as a means of suppressing the spallation mechanism.

Modeling the normal stress component σ_{22} evolution in pure bond coat TBCs using the higher-order theory produces results consistent with previous numerical studies reported in the literature. Specifically, in a pure bond coat TBC, the crest and trough of the wavy interface experience compression and tension, respectively, during initial heating; stress relaxation during the hold period produces stress reversal upon cooldown, resulting in tension and compression at the crest and trough. In heterogeneous bond coat TBCs with spatially uniform microstructure in the top coat/bond coat interfacial region, increasing the alumina particle content of the bond coat decreases this stress component at the wavy interface's crest at the expense of increased magnitude in the trough. Grading the heterogeneous bond coat microstructure from a high alumina content at the wavy interface's crest to low in the trough region makes it possible to manage stress magnitudes at both the crest and trough locations. However, the analysis based on homogenized properties of the het-

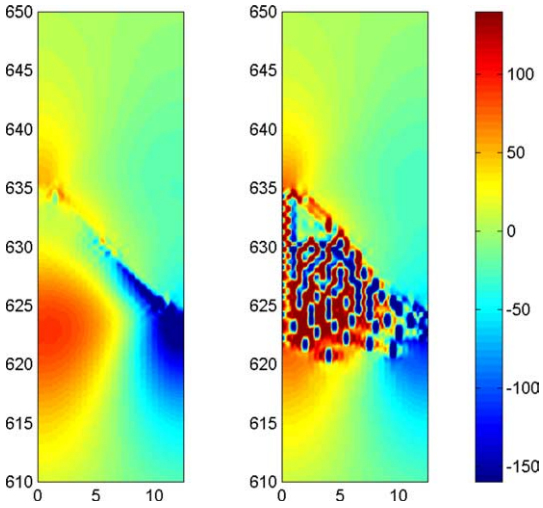

(a) Normal stress σ_{22} distributions.

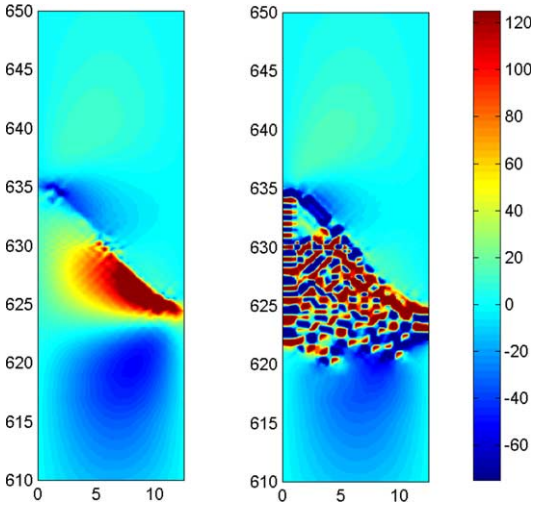

(b) Shear stress σ_{23} distributions.

Fig. 8. (a,b) Normal and shear stress distributions, σ_{22} (a) and σ_{23} (b), in the interfacial region of a graded bond coat TBC, with homogenized (left) and actual (right) microstructures, at the end of the first thermal cycle (colorbar scale in MPa).

erogeneous bond coat substantially overestimates the normal stress reduction at the crest in both spatially uniform and graded microstructure cases. Therefore, it does not appear that it is possible to reduce the normal stress component assumed to be responsible for the initiation of horizontal cracks to a sufficiently low level

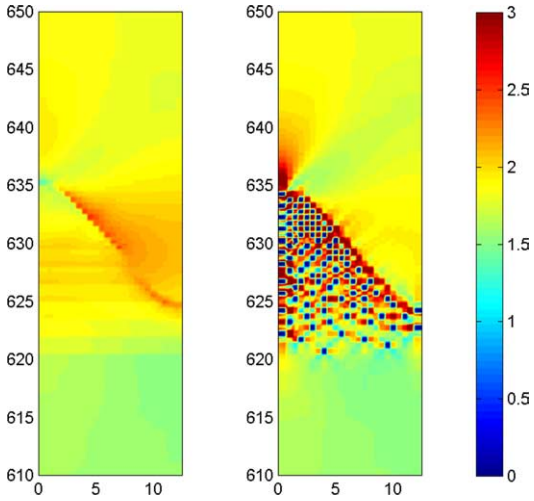

(c) Inelastic strain $\varepsilon_{\text{eff}}^{\text{int}}$ distributions.

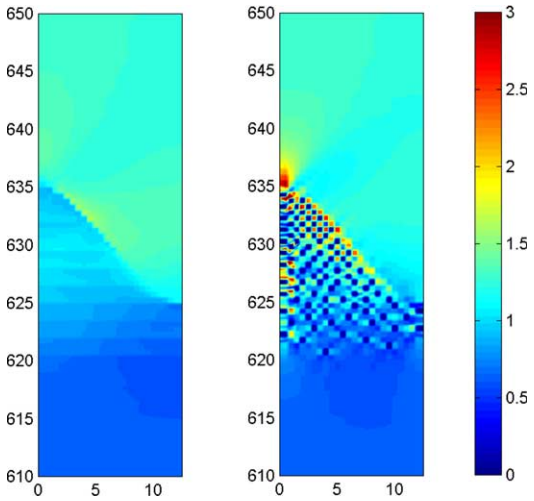

(d) Inelastic strain $\varepsilon_{\text{eff}}^{\text{res}}$ distributions.

Fig. 8. (c,d) Inelastic strain distributions, $\varepsilon_{\text{eff}}^{\text{int}}$ (c) and $\varepsilon_{\text{eff}}^{\text{res}}$ (d), in the interfacial region of a graded bond coat TBC, with homogenized (left) and actual (right) microstructures, at the end of the first thermal cycle (colorbar scale in % strain).

through the use of heterogeneous bond coats. The increase in coating durability reported by Brindley and co-workers for TBCs with two-phase microstructures cannot be explained by the type of mechanics-based mechanism investigated herein.

The results of this investigation also point to the important role that the shear stress component σ_{23}, thus far not extensively discussed, may play in the spallation

mechanism. Specifically, in a pure bond coat TBC, negative shear stress evolves in the top coat during initial heating, changing to positive upon cooldown due to relaxation during the hold period. However, the magnitude of this stress component is small relative to the normal stress σ_{22}. In the presence of bond coat heterogeneity, increasing the alumina particle content of the bond coat reverses the sign of the shear stress from positive to negative in the off-crest region and increases its magnitude and growth into the trough region. The shear stress magnitude in the off-crest location is substantially higher relative to that in the pure bond coat TBCs. In addition, homogenized analysis underestimates the magnitude of the shear stress in the off-crest region immediately adjacent to the top/bond coat interface, but overestimates the extent of its spread into the trough region. Thus the small reduction in the normal stress due to grading in the wavy interface crest neighborhood is offset by an increase in the magnitude of the shear stress in this location, thereby potentially promoting local crack initiation and growth through a mixed-mode mechanism.

Finally, the previously unreported evolution of inelastic strain fields presented herein reveals interesting trends that may be directly related to the initiation of horizontal cracks. In particular, in a pure bond coat TBC, substantial inelastic strain reversal occurs in the top and bond coats during thermal cycling. Further, residual inelastic strain build-up is observed in the wavy interface's crest region both on the top and bond coat sides. The inelastic behavior of the ceramic top coat is attributed to its porous microstructure characterized by the presence of dispersed microcracks. These microcracks provide the mechanism by which inelastic effects occur due to sliding of microcrack interfaces. This may lead to horizontal crack initiation in the presence of normal and shear stress components. In a heterogeneous bond coat TBC with spatially uniform microstructure in the top coat/bond coat interfacial region, the analysis based on homogenized bond coat properties predicts that increasing the alumina particle content of the bond coat reduces the inelastic strain accumulation at the crest while promoting its growth in the trough region. In contrast, the analysis based on actual bond coat properties indicates that the inelastic strain accumulation at the crest actually increases with increasing alumina particle content, with a smaller increase in the trough region. This is likely to accelerate the initiation of horizontal cracks due to fatigue-like damage of the porous top coat, a conclusion that cannot be deduced from the analysis based on homogenized bond coat properties.

The above discussion indicates that the use of heterogeneous bond coats is not likely to suppress the spallation mechanism caused by the initiation of horizontal cracks above crests of rough interfaces. Further, the evolution of the oxide film in the bond coat at the top/bond coat interface with time, not considered here, will amplify the effect of bond coat heterogeneity. That is, the normal stress suppression at the wavy interface's crest will be enhanced with increasing oxide film thickness, as will the magnitude of shear stress in the off-crest location in conjunction with its spread into the trough region, Pindera et al. (2003). The use of heterogeneous bond coats will thus not only accelerate the horizontal crack initiation, but also its growth. Due to the increasing importance of the shear stress component with increasing oxide film thickness, models for delamination growth based on mixed-mode fracture

mechanics therefore may be more appropriate than just Mode I considerations. However, such models must take into account the inelastic behavior of the porous ceramic top coat characterized by sliding of the microcrack interfaces. This behavior can be directly taken into account through explicit modeling of the actual top coat microstructure and the associated deformation mechanism, albeit at a substantial computational cost. An alternative and more efficient approach would involve the use of a coupled damage-viscoplasticity constitutive model at the macroscopic scale which becomes relevant under repeated loading (cf. Lemaitre and Chaboche, 1990; Voyiadjis et al., 1998). The substantial inelastic strain accumulation and reversal observed in our results would provide the mechanism by which a crack may grow in the presence of increasing shear stress field with increasing oxide film thickness. We note, in support of the shear stress contribution to the spallation mechanism, that experimental evidence exists which suggests that delamination growth in the top coat is not self-similar, i.e. it is not exclusively governed by Mode I consideration, but proceeds along a path characterized by deflections which conform to the overall shape of the rough interface, Singh et al. (2001).

We end this discussion by pointing out that in addition to the top/bond coat interface roughness, thermoinelastic parameter mismatch, oxide film thickness and top coat porosity, additional factors that may affect the spallation mechanism and ultimate failure modes of plasma-sprayed TBCs must be considered. These include: sintering of the top coat during exposure to high temperatures, Zhu and Miller (1998), which affects the thermomechanical coating properties, Zhu and Miller (2000), Thompson and Clyne (2001); and phase transitions occurring in the top and bond coat as well as in the thermally-grown oxide film, Alperine and Lelait (1994), leading to potential local degradation in the presence of large stresses that develop within the film itself, Christensen et al. (1996). The effect of the TBC constituent chemical composition on the oxide film adhesion is also an important consideration, Pint et al. (1998). Further, the magnitude of the applied thermal gradient and the coating surface temperature, not considered herein, has been demonstrated to have a direct influence on the TBC's durability, Koolloos et al. (1998). A comprehensive failure model for plasma-sprayed TBCs will accommodate all of these mechanisms. The theoretical framework of the higher-order theory employed in this investigation has the potential to do so.

6. Conclusions

The results generated using the higher-order theory for functionally graded materials indicate that, under spatially-uniform cyclic heating, the use of heterogeneous NiCrAlY bond coats containing a dispersion of alumina particles, aimed at reducing the top/bond coat thermal expansion mismatch in plasma-sprayed TBCs, is likely to accelerate the initiation of horizontal cracks in the top coat at, or just above, the rough interface's crests. These cracks are commonly assumed to be initiated by the relatively large normal stress at the crests of the rough top/bond coat interface which becomes tensile upon cooldown due to stress relaxation at elevated temperatures.

Our analysis predicts that the use of heterogeneous bond coats does not appreciably reduce the normal stress in the crest region of a rough interface if the actual bond coat microstructure is taken into account. In contrast, misleadingly appreciable normal stress reductions are predicted for a sufficiently large alumina particle content in the crest region by the analysis based on homogenized bond coat properties. Further, the magnitude of the thus-far neglected shear stress in the off-crest location of the rough interface's peak increases with increasing alumina particle content, which becomes substantially greater relative to that in the homogeneous bond coat case. This stress component is likely to accelerate the mixed-mode growth of horizontal cracks. Perhaps most significant is the pronounced increase in the evolution of inelastic strains with increasing alumina particle content in the crest location where horizontal cracks initiate. The evolution of inelastic strains is accompanied by inelastic strain reversal during thermal cycling, potentially accelerating crack initiation through microcrack coalescence. The analysis based on homogenized bond coat properties substantially underestimates the extent of the inelastic strain evolution, thereby leading to incorrect conclusions with regard to the effectiveness of heterogeneous bond coats in suppressing the initiation of horizontal cracks.

The above results thus indicate that micro-macrostructural coupling which explicitly accounts for particle–particle and particle–interface interactions, and which is an intrinsic feature of the higher-order theory, is important in the analysis of plasma-sprayed TBCs with heterogeneous bond coat microstructures. The micro-macrostructural coupling effects propagate sufficiently far into the top coat, modeled here as homogeneous, to affect the initiation of horizontal cracks and resulting crack-tip stress fields in the immediate vicinity of the top/bond coat interface. These results suggest that the porous microstructure of plasma-sprayed coatings, characterized by microcracks and splats of specific size, should be explicitly taken into account in order to gain a better understanding of the horizontal crack initiation and growth.

Acknowledgment

The first two authors gratefully acknowledge the support provided by the NASA-Glenn Research Center through the NASA Grant NAG3-2359.

References

Aboudi, J., 1995. Micromechanical analysis of thermo-inelastic multiphase short-fiber composites. Composites Engineering 5 (7), 839–850.

Aboudi, J., Pindera, M.-J., Arnold, S.M., 1999. Higher-order theory for functionally graded materials. Composites: Part B (Engineering) 30 (8), 777–832.

Aboudi, J., Pindera, M.-J., Arnold, S.M., 2003. Higher-order theory for periodic multiphase materials with inelastic phases. International Journal of Plasticity 19 (6), 805–847.

Ali, M.Y., Nusier, S.Q., Newaz, G.M., 2001. Mechanics of damage initiation and growth in a TBC/superalloy system. International Journal of Solids and Structures 38, 3329–3340.

Alperine, S., Lelait, L., 1994. Microstructural investigations of plasma-sprayed yttria partially stabilized zirconia TBC. ASME Journal of Engineering for Gas Turbines and Power 116, 258–265.

Bansal, Y., Pindera, M.-J., 2003. Efficient reformulation of the thermoelastic higher-order theory for FGMs. Journal of Thermal Stresses 26 (11-12), 1–38, See also: NASA Contractor Report 2002-211909, November 2002.

Brindley, W.J., Miller, R.A., Aikin, B.J., 1998. Improved bond-coat layers for thermal-barrier coatings. NASA Tech Briefs August, 63–65.

Chang, G.C., Phucharoen, W., Miller, R.A., 1987. Behavior of thermal barrier coatings for advanced gas turbine blades. Surface and Coatings Technology 30, 13–28.

Christensen, R.J., Lipkin, D.M., Clarke, D.R., 1996. Nondestructive evaluation of the oxidation stresses through thermal barrier coatings using Cr^{3+} piezospectroscopy. Applied Physics Letters 69 (24), 3754–3756.

Crossman, F.W., Karlak, R.K., Barnett, D.M., 1974. Creep of B/Al composites as influenced by residual stress, bond strength, and fiber packing geometry. In: Failure Modes in Composites II. TMS of AIME Publication, New York, pp. 8–31.

Crossman, F.W., Karlak, R.K., 1976. Multiaxial creep of metal matrix fiber reinforced composites. In: Failure Modes in Composites III. TMS of AIME Publication, New York, pp. 260–287.

DiMassi-Marcin, J.T., Sheffler, K.D., Bose, S., 1990. Mechanisms of degradation and failure in a plasma-deposited thermal barrier coating. Journal of Engineering for Gas Turbines and Power 112, 521–526.

Evans, A.G., Crumley, G.B., Demaray, R.R., 1983. On the mechanical behavior of brittle coatings and layers. Oxidation of Metals 20 (5/6), 193–216.

Freborg, A.M., Ferguson, B.L., Brindley, W.J., Petrus, G.J., 1998. Modeling oxidation induced stresses in thermal barrier coatings. Materials Science & Engineering A245, 182–190.

Kim, J.H., Paulino, G.H., 2003. An accurate scheme for mixed-mode fracture analysis of functionally graded materials using the interaction integral and micromechanics models. International Journal for Numerical Methods in Engineering 58 (10), 1457–1497.

Koolloos, M.F., Liempd, G.G., Houben, J.M., 1998. Effect of local thermal shock load on plasma sprayed thermal barrier coatings. Surface Engineering 14 (2), 144–148.

Lemaitre, J., Chaboche, J.-L., 1990. Mechanics of Solid Materials. Cambridge University Press, Cambridge.

Miller, R.A., Lowell, C.E., 1982. Failure mechanisms of thermal barrier coatings exposed to elevated temperatures. Thin Solid Films 95, 265–273.

Ostoja-Starzewski, M., in this issue. Plasticity of random media: status and challenges. International Journal of Plasticity.

Paulino, G.H., Fannjiang, A.C., Chan, Y.C., 2003. Gradient elasticity theory for mode III fracture in functionally graded materials – Part I: Crack perpendicular to the material gradation. Journal of Applied Mechanics 70 (4), 531–542.

Petrus, G.J., Ferguson, B.L., 1997. A software tool to design thermal barrier coatings: a technical note. Journal of Thermal Spray Technology 6 (1), 29–34, See also: NASA Phase I Final Report, Project No. 93-1-04-23-8477.

Pindera, M-J., Arnold, S.M., Williams, T.O., 1994. Thermoplastic response of metal matrix composites with homogenized and functionally graded interfaces. Composites Engineering 4 (1), 129–145.

Pindera, M-J., Aboudi, J., Arnold, S.M., 1995. Limitations of the uncoupled, RVE-based micromechanical approach in the analysis of functionally graded composites. Mechanics of Materials 20 (1), 77–94.

Pindera, M.-J., Aboudi, J., Arnold, S.M., 2000. The effect of interface roughness and oxide film thickness on the inelastic response of thermal barrier coatings to thermal cycling. Materials Science & Engineering A284, 158–175.

Pindera, M.-J., Aboudi, J., Arnold, S.M., 2003. Analysis of TBCs with homogeneous and heterogeneous bond coats under spatially uniform cyclic thermal loading. NASA Technical Memorandum 2003-210803, NASA-Glenn Research Center, Cleveland. See also: Engineering Fracture Mechanics 69, 2002, 1587–1606.

Pint, B.A., Wright, I.G., Lee, W.Y., Zhang, Y., Prussner, K., Alexander, K.B., 1998. Substrate and bond coat compositions: factors affecting alumina scale adhesion. Materials Science and Engineering A245, 201–211.

Sheffler, K.D., Gupta, D.K., 1988. Current status and future trends in turbine application of thermal barrier coatings. ASME Journal of Engineering For Gas Turbines and Power 110, 605–609.

Singh, J.P., Nair, B.G., Renusch, D.P., Sutaria, M.P., Grimsditch., M.H., 2001. Damage evolution and stress analysis in zirconia thermal barrier coatings during cyclic and isothermal oxidation. Journal of American Ceramic Society 84 (10), 2385–2393.

Strangman, T.E., 1985. Thermal barrier coatings for turbine airfoils. Thin Solid Films 127, 93–105.

Thompson, J.A., Clyne, T.W., 2001. The effect of heat treatment on the stiffness of zirconia top coats in plasma-sprayed TBCs. Acta Materialia 49, 1565–1575.

Voyiadjis, G.Z., Ju, J.-W., Chaboche, J.-L., 1998. Damage Mechanics in Engineering Materials. Elsevier, New York.

Zhu, D., Miller, R.A., 1998. Sintering and creep behavior of plasma-sprayed zirconia and hafnia based thermal barrier coatings. NASA TM 1998-208406.

Zhu, D., Miller, R.A., 2000. Thermal conductivity and elastic modulus evolution of thermal barrier coatings under high heat flux conditions. Journal of Thermal Spray Technology 9 (2), 175–180.